Research Square

Preprints are preliminary reports that have not undergone peer review.
They should not be considered conclusive, used to inform clinical practice,
or referenced by the media as validated information.

Integrated Multi-Omics and Machine Learning Identify PTTG1 as a Prognostic Biomarker and Therapeutic Target in Endometrial Cancer

Dilimulati Yalikun
the First Affiliated Hospital of Zhengzhou University
Lulu Si
the First Affiliated Hospital of Zhengzhou University
Guo Zheng
the First Affiliated Hospital of Zhengzhou University
Yuxi Jin
the First Affiliated Hospital of Zhengzhou University
Hanlin Fu
the First Affiliated Hospital of Zhengzhou University
Ruixia Guo
grxcdxzzu@163.com

the First Affiliated Hospital of Zhengzhou University

Article

Keywords: Endometrial carcinoma, PTTG1, Machine Learning, Single-cell RNA sequencing, Spatial transcriptomics, Tumor immune microenvironment

Posted Date: November 3rd, 2026

DOI: https://doi.org/10.21203/rs.3.rs-10764988/v1

License: This work is licensed under a Creative Commons Attribution 4.0 International License.
Read Full License

Additional Declarations: No competing interests reported.

Integrated Multi-Omics and Machine Learning Identify PTTG1 as a Prognostic Biomarker and Therapeutic Target in Endometrial Cancer

Dilimulati Yalikun[1], Lulu Si[1], Guo Zheng[1], Yuxi Jin[1], Hanlin Fu[1], Ruixia Guo[1, *]

[1] Department of Gynecology, the First Affiliated Hospital of Zhengzhou University, Zhengzhou city, Henan province,450000, China

Dilimulati Yalikun, dilmuratyalkun@gs.zzu.edu.cn

Lulu Si, silulu2006324@163.com

Guo Zheng, zhengguotx@163.com

Yuxi Jin, jinyuxi1303@163.com

Hanlin Fu, 69440089@qq.com

[*]Corresponding author: Ruixia Guo, grxcdxzzu@163.com

Abstract

Background: Endometrial carcinoma (UCEC) exhibits high molecular heterogeneity, and the lack of precise prognostic biomarkers and therapeutic targets severely limits the clinical management of high-risk patients. This study aimed to identify a robust multi-omics biomarker and elucidate its intrinsic oncogenic mechanisms and extrinsic immune-remodeling roles in the UCEC microenvironment.

Methods: We systematically integrated transcriptomic data from TCGA and GEO cohorts. WGCNA coupled with four machine learning algorithms (LASSO, SVM-RFE, XGBoost, Boruta) were employed for feature selection. Single-cell RNA sequencing and spatial transcriptomics were integrated to map the cellular landscape. In silico virtual knockout, virtual overexpression, and pharmacogenomic analyses were conducted. Computational predictions were experimentally validated using Western blot, qRT-PCR, and immunohistochemistry in paired clinical specimens, and corroborated by CPTAC proteomic analysis.

Results: PTTG1 was identified as an independent prognostic biomarker, with significant overexpression confirmed at both mRNA and protein levels and predominant nuclear localization in tumor epithelium. Mechanistically, virtual knockout revealed PTTG1 drives malignant progression through hyperactivation of cell cycle, ribosome biogenesis, and glutathione metabolism, whereas virtual overexpression activated immune-related transcriptional networks including MHC class II antigen presentation. Integrated scRNA-seq and spatial transcriptomics demonstrated PTTG1 enrichment in malignant epithelial cells and tumor-associated macrophages. Drug sensitivity predictions identified selective vulnerability to MEK inhibitors, including selumetinib and trametinib.

Conclusion: PTTG1 serves as a multidimensional oncogenic driver and independent prognostic biomarker in UCEC, intrinsically fueling tumor proliferation while extrinsically orchestrating an

immunosuppressive microenvironment. Bidirectional in silico perturbation revealed distinct transcriptional consequences, substantiated by multi-level experimental validation. Drug sensitivity predictions identified selective MEK inhibitor vulnerabilities, providing a rationale for PTTG1-guided prognostic stratification and targeted therapeutic strategies in high-risk UCEC.

Keywords: Endometrial carcinoma; PTTG1; Machine Learning; Single-cell RNA sequencing; Spatial transcriptomics; Tumor immune microenvironment.

Background

Uterine corpus endometrial carcinoma (UCEC) is one of the most prevalent gynecological malignancies globally, with a continuously rising incidence and mortality rate in recent years[1]. While early-stage UCEC patients generally exhibit favorable outcomes following standard surgical resection, the prognosis for patients with advanced, recurrent, or metastatic disease remains unacceptably poor[2–4]. This clinical dilemma is predominantly attributed to the high molecular and spatial heterogeneity inherent to UCEC tumors, which limits the efficacy of conventional chemotherapy and radiotherapy. Consequently, there is an urgent and unmet clinical need to identify highly robust prognostic biomarkers and explore actionable therapeutic targets to improve the personalized management of UCEC patients.

The progression of UCEC is driven not only by the intrinsic genetic and epigenetic alterations within malignant epithelial cells but also by the complex interactions within the tumor immune microenvironment (TIME)[5–7]. The TIME of UCEC is highly dynamic ecosystem composed of stromal components, extracellular matrix, and various infiltrating immune cells, notably tumor-associated macrophages (TAMs), regulatory T cells (Tregs), natural killer (NK) cells[8]. Recent multi-omics studies have highlighted that TAMs, which often polarize toward an immunosuppressive M2-like phenotype, play a pivotal role in remodeling the extracellular matrix, promoting tumor angiogenesis, and establishing an “immune desert” or “cold” tumor phenotype[9]. This highly immunosuppressive microenvironment severely dampens anti-tumor immune surveillance and acts as a major barrier to the efficacy of emerging immunotherapies, particularly immune checkpoint blockades (ICBs)[10,11,12]. However, only a limited subset of UCEC patients derive durable clinical benefits. Traditional bulk RNA sequencing (RNA-seq) has provided valuable insights into tumor transcriptomics, but it fundamentally obscures cellular heterogeneity by averaging out expression signals across diverse cell populations. The advent of single-cell RNA sequencing (scRNA-seq) and spatial transcriptomics (ST) has revolutionized our ability to dissect the TIME at unprecedented resolution, enabling the precise mapping of oncogenic drivers and their intricate crosstalk with immune cells, such as tumor-associated macrophages, within their native architectural context[13].

To systematically mine core prognostic drivers from massive transcriptomic datasets, advanced machine learning algorithms have proven to be highly efficient and robust[14]. In this context, Pituitary tumor-transforming gene 1 (PTTG1), originally identified as a pivotal mammalian securin protein, has garnered significant attention. Physiologically, PTTG1 plays an indispensable role in maintaining genomic stability by tightly regulating sister chromatid segregation during the mitotic

anaphase[15–17]. However, beyond its cell cycle functions, accumulating multi-dimensional evidence has firmly established PTTG1 as a potent oncogene across a broad spectrum of human malignancies. Aberrant overexpression of PTTG1 has been frequently documented in diverse solid tumors, including breast cancer[18], hepatocellular carcinoma[19,20], colorectal cancer[21], lung adenocarcinoma[22], and pituitary adenomas[23], where its elevated levels robustly correlate with aggressive clinicopathological traits, tumor immune evasion, and poor clinical outcomes[24,25].

Mechanistically, contemporary oncological research highlights that PTTG1 serves as a central orchestrator of malignant progression. It actively drives tumor hyperproliferation, facilitates epithelial-mesenchymal transition (EMT) to promote distant metastasis, and stimulates tumor angiogenesis through the transactivation of downstream signaling cascades, such as the PI3K/AKT, MAPK, and c-Myc pathways[24,26]. Furthermore, emerging evidence suggests that PTTG1 is deeply involved in remodeling tumor cellular metabolism and overriding DNA damage repair checkpoints, endowing cancer cells with enhanced survival advantages and profound therapeutic resistance[27]. Despite these extensive pan-cancer insights, the precise prognostic landscape, cell-intrinsic multi-omics dependencies, and spatial-temporal dynamics of PTTG1 specifically within the UCEC immune microenvironment remain largely elusive.

To address these critical knowledge gaps, the present study employed a comprehensive integrative framework. By systematically combining bulk RNA-seq cohorts, WGCNA, and four distinct machine learning algorithms (LASSO, SVM-RFE, XGBoost, and Boruta), rigorously screened and identified PTTG1 as a core independent prognostic biomarker for UCEC. Furthermore, integrating scRNA-seq and spatial transcriptomics, combined with an in silico virtual simulation and pharmacogenomic profiling, we aimed to decipher the exact cellular origins, internal downstream regulatory mechanisms, and extrinsic immune-remodeling functions of PTTG1. Ultimately, our study seeks to provide a multidimensional understanding of PTTG1 and offer insights into personalized risk stratification and targeted interventions for high-risk UCEC patients.

Methods

Data Acquisition and Preprocessing

Publicly available transcriptomic and clinical data of UCEC were systematically collected from multiple databases. The RNA sequencing (RNA-seq) data (Transcripts Per Million, TPM format) and corresponding clinical metadata for the TCGA-UCEC cohort were downloaded from the UCSC Xena browser (https://xenabrowser.net/). Additionally, independent microarray datasets (GSE17025, GSE115810, GSE63678) along with their clinical annotations were obtained from the Gene Expression Omnibus (GEO) database (https://www.ncbi.nlm.nih.gov/geo/). Additionally, single-cell RNA sequencing data (GSE173682, 5 UCEC samples) and spatial transcriptomics data (GSE203612, UCEC tissue sections) were also obtained from the GEO database. Detailed information is presented in Table 1.

To integrate the three training GEO datasets (GSE17025, GSE115810, GSE63678) and minimize systematic errors caused by different experimental platforms and batches, batch effect correction

was performed using the removeBatchEffect function from the limma package, with auxiliary adjustment by the sva package. Batch information was extracted from the original dataset metadata and set as a covariate in the correction model. Boxplots and principal component analysis (PCA) scatter plots were generated using the ggplot2 and FactoMineR packages before and after batch correction to visualize the correction effect. Boxplots were used to display the distribution of gene expression values across samples, while PCA plots (based on the first two principal components) illustrated sample clustering to confirm the elimination of batch effects and clear separation between tumor and normal samples.

Table 1 Characteristics of multiple datasets used in this study：

Dataset ID	Platform	Sample type	Sample size (Tumor/Normal)
GSE17025	Bulk microarray	Endometrial tissue	103（91/12）
GSE115810	Bulk microarray	Endometrial tissue	27（24/3）
GSE63678	Bulk microarray	Endometrial tissue	12（7/5）
TCGA-UCEC	Bulk RNA-seq	Endometrial tissue	589（554/35）
GSE173682	scRNA-seq	Endometrial tissue	5 tumor tissues
GSE203612	Spatial transcriptomics	Endometrial tissue	1 tumor tissue

Differentially Expressed Genes Screening and WGCNA

Differential expression analysis (DEA) was performed on the batch-corrected integrated GEO dataset using the limma package. For GEO datasets, background correction and normalization were conducted prior to DEA to construct high-quality expression matrices. Linear models were fitted using the lmFit function, followed by Bayesian correction with the eBayes function to compute differential expression statistics. Differentially expressed genes (DEGs) were identified with the cutoff criteria of $|\log_2 \text{fold change (FC)}| > 1$ and adjusted p-value (adj. P. Val) < 0.05.

Subsequently, to explore the highly coordinated gene networks, Weighted Gene Co-expression Network Analysis (WGCNA) was performed using the WGCNA R package. First, the hierarchical clustering function was used to detect and remove outlier samples. A soft-thresholding power β was calculated and selected to ensure a scale-free network topology ($R^2 > 0.85$). The adjacency matrix was then transformed into a Topological Overlap Matrix (TOM) to evaluate network interconnection. Modules containing highly correlated genes were assigned to different colors using the dynamic tree cut algorithm. The correlations between module eigengenes (MEs) and clinical traits were computed. The module with the highest significance for UCEC was defined as the key module. Finally, the intersecting genes between the DEGs and the key WGCNA module were extracted as core candidate genes for further feature selection.

Functional Enrichment Analysis

To explore the underlying biological functions and signaling pathways of the consensus candidate genes, Gene Ontology (GO) and Kyoto Encyclopedia of Genes and Genomes (KEGG) pathway enrichment analyses were conducted using the clusterProfiler, org.Hs.eg.db, and enrichplot packages in R. Initially, gene symbols were converted to Entrez IDs to generate the input gene list. The

GO enrichment analysis comprehensively covered three categories: biological processes (BP), cellular components (CC), and molecular functions (MF), utilizing the enrichGO function. Significant enrichment terms were selected based on a p-value < 0.05 and a q-value < 0.05. Concurrently, KEGG pathway enrichment analysis was performed using the enrichKEGG function against the KEGG database (https://www.kegg.jp/)[28,29], with the human genome serving as the reference, applying the same statistical thresholds. Finally, the results were visualized as bar plots displaying the top enriched pathways, sorted by gene ratio, to intuitively present the functional characteristics of the consensus DEGs. Permission for the use of the KEGG pathway database in this publication has been obtained from the Kanehisa laboratories.

Machine Learning -Based Core Gene Screening

To identify the most biologically and clinically relevant core genes from the consensus DEGs, four complementary machine learning algorithms were employed: LASSO Regression, Support Vector Machine-Recursive Feature Elimination (SVM-RFE), XGBoost, and Boruta. The expression matrix of consensus DEGs and corresponding sample grouping information (tumor/normal) were standardized using the scale function to ensure the stability of model training. The glmnet package was used to perform LASSO regression. 5-fold cross-validation was applied to determine the optimal penalty parameter λ (lambda.min), and genes with non-zero coefficients after LASSO shrinkage were selected as candidate genes. The e1071 and caret packages were used to implement SVM-RFE. The radial basis function (RBF) was set as the kernel function, and the algorithm iteratively eliminated features with the lowest importance scores until the optimal feature subset was obtained (determined by peak cross-validation accuracy). The xgboost package was used to construct the extreme gradient boosting tree model. Feature importance was evaluated by the gain value (reflecting the total contribution of a feature to model performance), and genes with top importance scores were selected as candidates. The Boruta package was used for stable feature selection. This algorithm generates random shadow features (permutations of real features) to compare with genuine features. Genes with a mean Z-score significantly higher than the maximum Z-score of shadow features were retained as candidate genes, ensuring the stability of selected features. The VennDiagram package was used to identify the intersection of candidate genes selected by all four algorithms, which were defined as the final core genes of UCEC. This multi-algorithm cross-validation strategy minimized model bias and overfitting, ensuring the robustness of core genes.

Expression and Prognostic Value of Core Genes

To further validate the clinical significance of the five consensus core genes (PNP, CDC20, PTTG1, S100A11, and KLF5) identified by the machine learning algorithms, their expression patterns, diagnostic efficacy, and prognostic values were systematically evaluated using the TCGA-UCEC dataset. First, the differential expression levels of these five genes between UCEC tumor tissues and adjacent normal tissues were analyzed using the Wilcoxon rank-sum test. The log2 fold-change (log2FC) and corresponding p-values were calculated and visualized via boxplots. Subsequently, to assess the diagnostic accuracy of these core genes in distinguishing tumor samples from normal tissues, Receiver Operating Characteristic (ROC) curves were constructed, and the Area Under the

Curve (AUC) along with 95% Confidence Intervals (CIs) were calculated using the pROC function of R package. To determine the long-term prognostic significance of these genes, Kaplan-Meier (K-M) survival analyses for both overall survival (OS) and progression-free interval (PFI) were conducted using the TCGA-UCEC clinical annotation. UCEC patients were stratified into high-expression and low-expression cohorts based on the median expression value of each respective gene. Survival curves were generated using the survival and survminer R packages, and statistical differences between the strata were evaluated via the log-rank test. Hazard Ratios (HR) and 95% CIs were computed using univariate Cox proportional hazards regression. Only the gene that demonstrated statistically significant associations with both OS and PFI ($p < 0.05$), alongside robust diagnostic and differential expression profiles, was selected as the ultimate independent prognostic biomarker for subsequent downstream multi-omics and mechanism analyses.

Clinicopathological Correlation Analysis of PTTG1

To evaluate the clinical relevance of PTTG1 in UCEC, the correlation between PTTG1 expression levels and various clinicopathological characteristics of patients within the TCGA-UCEC cohort was systematically analyzed. The clinical traits evaluated included patient age, FIGO stage, histological grade, BMI (body mass index) and primary tumor classification, among others. For clinical variables stratified into two distinct groups, the Wilcoxon rank-sum test was employed to assess the statistical significance of the differences in PTTG1 expression. For variables with multiple categories (such as FIGO stages I, II, III, and IV, or histological grades 1, 2, and 3), the Kruskal-Wallis test was applied for multi-group comparisons. Pairwise post-hoc comparisons were subsequently conducted to identify specific inter-group differences. All statistical analyses were two-tailed, and a p-value < 0.05 was considered statistically significant. The clinical correlation landscapes were visualized as boxplots or violin plots using the ggplot2 and ggpubr R packages.

Single gene Co-expression Network and Functional Enrichment Analysis

To explore the underlying biological mechanisms and regulatory networks mediated by PTTG1 in UCEC, a gene co-expression analysis was conducted. The Spearman correlation coefficients between the mRNA expression levels of PTTG1 and all other genes within the TCGA-UCEC cohort were systematically calculated. Genes significantly correlated with PTTG1 were identified based on strict statistical thresholds ($|\text{Spearman r}| > 0.4$ and $p < 0.05$). The top highly positively and negatively co-expressed genes were selected, and their linear relationships with PTTG1 were visualized using scatter plots equipped with regression lines and confidence intervals via the ggplot2 and ggpubr R packages. Subsequently, to decipher the downstream biological functions and signaling cascades associated with this PTTG1-driven co-expression network, GO and KEGG enrichment analyses were performed on the significantly co-expressed genes. A statistical significance threshold of p-value < 0.05 was applied. The top enriched functional terms were visualized using bar plots to intuitively delineate the molecular mechanisms, such as cell cycle regulation and mitotic chromosomal segregation, orchestrated by PTTG1. To capture pathway-level transcriptional shifts driven by PTTG1 expression, Gene Set Enrichment Analysis (GSEA) was performed using the clusterProfiler package. TCGA-UCEC patients were stratified into PTTG1-high and

PTTG1-low groups by median expression. All genes were ranked by $\log_2$ fold change between groups, and enrichment was evaluated against the MSigDB KEGG legacy gene sets (v2025.1). Pathways with an FDR-adjusted p-value < 0.05 were considered significant. NES > 0 indicated activation in the PTTG1-high group, and NES < 0 indicated activation in the PTTG1-low group.

Tumor Immune Microenvironment Evaluation

To comprehensively evaluate the association between PTTG1 expression and the tumor immune microenvironment (TIME) in UCEC, both macroscopic and microscopic immune infiltration analyses were performed. At the macroscopic level, the ESTIMATE (Estimation of STromal and Immune cells in tumor tissues using expression data) algorithm was utilized via the estimate R package to infer the overall infiltration of non-tumor cells. For each UCEC sample, the Stromal Score, Immune Score, and ESTIMATE Score were calculated based on specific gene expression signatures, which inversely reflected the tumor purity. Differences in these microenvironmental scores between the PTTG1-high and PTTG1-low expression groups (stratified by the median value) were evaluated using the Wilcoxon rank-sum test. At the microscopic level, the relative proportions of 22 distinct immune cell types within the TCGA-UCEC cohort were quantified using the CIBERSORT (Cell-type Identification by Estimating Relative Subsets of RNA Transcripts) deconvolution algorithm with 1,000 permutations. To ensure the reliability of the immune cell estimation, only samples with a CIBERSORT output of p-value < 0.05 were included in the subsequent comparative analysis. The correlation between PTTG1 expression and the abundance of individual infiltrating immune cell types (such as macrophages) was assessed using Spearman correlation analysis. Furthermore, differences in immune cell fractions between the PTTG1-high and PTTG1-low groups were compared using the Wilcoxon rank-sum test. All microenvironmental landscapes and correlation profiles were visualized using the ggplot2 and ggpubr R packages.

Drug Sensitivity and Targeted Therapy Prediction

To translate our molecular findings into potential clinical applications, we evaluated the differences in chemotherapeutic and targeted drug sensitivity among UCEC patients based on their PTTG1 expression profiles. The half-maximal inhibitory concentration (IC50) values for a wide array of anti-cancer compounds were imputed for each patient in the TCGA-UCEC cohort using the oncoPredict R package, which represents an advanced machine-learning framework for in vivo drug response prediction. The extensive pharmacogenomic training datasets, including the Genomics of Drug Sensitivity in Cancer (GDSC), were utilized as reference baselines. The predicted IC50 values inversely correlate with drug sensitivity, lower IC50 scores indicate a higher predicted sensitivity (efficacy) to the specific agent. Statistical differences in the predicted IC50 values between the PTTG1-high and PTTG1-low expression groups were evaluated using the Wilcoxon rank-sum test. Furthermore, Spearman correlation analysis was conducted to establish the continuous linear relationship between PTTG1 mRNA expression levels and drug sensitivity scores. The key identified targeted therapies (e.g., MEK inhibitors such as Selumetinib and Trametinib) demonstrating significantly different efficacies across groups were visualized via boxplots using the ggplot2 and ggpubr packages.

Single-Cell RNA Sequencing Analysis

To characterize the cellular heterogeneity and precise origin of PTTG1 expression in UCEC, the raw scRNA-seq dataset GSE173682, consisting of 5 clinical UCEC tissue samples, was downloaded from the GEO database. Data analysis was primarily executed using the Seurat (v5) R package. Strict quality control (QC) filters were applied to eliminate low-quality cells or doublets. Cells were retained for downstream analysis only if they met the following criteria: (1) number of detected genes (Features) between 300 and 6,000; (2) total RNA counts between 1,000 and 40,000; (3) percentage of mitochondrial gene expressions (percent.mt) < 20%; (4) percentage of erythrocyte gene expressions (percent.HB) < 1%. Following QC, the data were normalized using the NormalizeData function, and the top 3,000 highly variable genes (HVGs) were identified via the FindVariableFeatures function using the vst method. To integrate the samples and eliminate potential non-biological patient-specific batch effects, the Harmony algorithm was implemented via the harmony R package, using the patient identity (orig.ident) as the grouping variable. Principal Component Analysis (PCA) was performed on the integrated matrix, and the top 30 principal components (PCs) were selected for graph-based clustering (FindNeighbors and FindClusters functions) and non-linear dimensionality reduction via Uniform Manifold Approximation and Projection (UMAP). Major cell lineages were comprehensively annotated into eight distinct types—Fibroblasts, T cells, Epithelial cells, Endothelial cells, Macrophages, NK cells, B cells, and Mast cells—based on Canonical Cell Type Marker Genes. The expression percentage and specific intensity of PTTG1 across individual clusters and designated cell lineages were determined and visualized using feature plots and violin plots. To investigate intercellular communication networks, the CellChat R package was employed. Ligand-receptor interactions were inferred from the scRNA-seq data using the curated CellChatDB database. The number and strength of signaling interactions among the eight annotated cell types were calculated and visualized as circle plots and bar plots.

Spatial Transcriptomics Analysis and Spatial Mapping

To validate the spatial distribution and architectural localization of PTTG1 within the native tumor context, the spatial transcriptomics dataset GSE203612 was acquired from the GEO database. ST data processing, alignment, and visualization were performed utilizing the Seurat framework. The raw spatial expression counts were normalized and variance-stabilized using the SCTransform function to account for technical variations across spatial spots while preserving biological signals. Dimensionality reduction was performed using PCA, and unsupervised clustering was carried out to identify spatially distinct tissue domains. Corresponding Hematoxylin and Eosin (H&E) histological staining images were utilized to register and align the spatial coordinate matrix. The scRNA-seq annotated cell type signatures were projected onto the ST tissue sections to map the spatial organization of the UCEC microenvironment. Finally, the spatial feature plot function was utilized to visualize the in situ physical expression intensity and topographical coordinates of PTTG1 across the tissue landscape, allowing direct correlation with tumor parenchymal and stromal boundaries.

In Silico (Virtual) Knockout Analysis of PTTG1

To decipher the direct causal regulatory network and functional dependencies governed by PTTG1 at single-cell resolution, an in silico virtual knockout analysis was conducted using the processed scRNA-seq expression matrix. The network-based perturbation simulation was performed via the scTenifoldKnock pipeline[30]. Briefly, a single-cell gene regulatory network (scGRN) was constructed for the target cell populations using a multi-layer tensor decomposition approach based on consensus conditional mutual information. To simulate the biological knockout of PTTG1, its corresponding row and column profiles within the adjacency matrix of the control network were synthetically set to zero, generating a perturbed (knockout) network. The structural divergence and edge-weight distances between the wild-type control network and the PTTG1-knockout network were quantified. The systemic gene-specific perturbation levels were mathematically evaluated and normalized into Z-scores. Genes with significantly high absolute Z-scores were identified as critical downstream targets responsive to PTTG1 depletion. To identify the specific biological vulnerabilities and metabolic pathways modulated by PTTG1, the top perturbed genes were subjected to GO and KEGG functional enrichment analyses using the clusterProfiler R package, as described previously.

Virtual Overexpression Analysis of PTTG1

To complement the virtual knockout and explore the gain-of-function consequences of PTTG1, a virtual overexpression analysis was performed using the scTenifoldNet framework[31]. While the virtual knockout simulates PTTG1 depletion, the virtual overexpression models the transcriptional network perturbation induced by PTTG1 upregulation. Using the same scRNA-seq expression matrix described above, a wild-type (WT) single-cell gene regulatory network (scGRN) was constructed via multi-layer tensor decomposition (nNet = 10, nCells = 500, nComp = 3). To simulate PTTG1 overexpression, the row profile corresponding to PTTG1 in the adjacency matrix was artificially amplified by a factor of 100 with an additive constant of 10, generating the overexpressed (OE) network. Manifold alignment was then performed to align the WT and OE networks, and the dRegulation function was applied to quantify gene-specific perturbation magnitudes as Z-scores and fold changes (FC). Significantly perturbed genes were identified using an adjusted p-value (Benjamini-Hochberg false discovery rate) threshold of < 0.05. The biological functions and signaling pathways enriched among the perturbed genes were subsequently characterized via GO and KEGG enrichment analyses using the clusterProfiler R package.

Experimental Validation

Tissue Specimen Collection

Six paired fresh-frozen tumor tissues and matched adjacent normal endometrial tissues (>2 cm from the tumor margin, histologically confirmed tumor-free) were obtained from patients who underwent total hysterectomy at First Affiliated Hospital of Zhengzhou University between January 2025 and March 2025. None of the patients had received preoperative radiotherapy, chemotherapy, or hormonal therapy. Written informed consent was obtained from all participants, and the study was approved by the Institutional Ethics Committee of first affiliated hospital of Zhengzhou University (Approval No: 2025-KY-0029). All tissue specimens were immediately snap-

frozen in liquid nitrogen after surgical resection and stored at −80°C until use. The same six paired specimens were used for both Western blot and qRT-PCR analyses to enable direct cross-method comparison. For immunohistochemistry (IHC) staining, formalin-fixed paraffin-embedded (FFPE) tissue blocks from five paired UCEC tumor and adjacent normal endometrial tissues were collected from the same institutional cohort under identical inclusion criteria and ethical approval.

Western Blot Analysis

Total protein was extracted from the above tissue specimens (approximately 50 mg each) using RIPA lysis buffer (R0010, Solarbio, China) supplemented with 1 mM phenylmethylsulfonyl fluoride (PMSF) and protease inhibitor cocktail (P0100, Solarbio, China). Protein concentrations were quantified using the BCA Protein Assay Kit (PC0020, Solarbio, China). Equal amounts of protein (30 μg per lane) were separated by 12% SDS-PAGE and transferred onto Nitrocellulose membranes (0.42μm, HATF00010, Merck Millipore,Ireland). Membranes were blocked with protein-free rapid blocking buffer (Servicebio, G2052-500ML, Wuhan, China) at room temperature for 30 minutes, followed by overnight incubation at 4°C with primary antibodies against PTTG1 (rabbit monoclonal antibody, 1:1000; Proteintech, 18040-1-AP, China) and β-actin (mouse Recombinant Anti-β-actin antibody, 1:5000; AC240324001, Servicebio, UK). After washing with TBST, membranes were incubated with HRP-conjugated goat anti-rabbit and goat anti-mouse secondary antibodies (1:2000; Proteintech, RGAR001/ RGAM001, China) at room temperature for 2 hours. Protein bands were visualized using ECL substrate (Millipore, WBKLS0500, USA) and detected with the ChemiDoc XRS+ imaging system (Bio-Rad, USA). Densitometric quantification was performed using ImageJ software (NIH, USA), with PTTG1 band intensity normalized to β-actin.

RNA Extraction and Quantitative Real-Time PCR

Total RNA was extracted from the same six paired frozen tissue specimens (30 mg each) using TRIzol Reagent (15596018CN, Thermo, USA) according to the manufacturer's protocol. Briefly, tissues were homogenized in 1 mL TRIzol, followed by phase separation with chloroform and isopropanol precipitation. RNA pellets were washed with 75% ethanol, air-dried, and dissolved in RNase-free water. RNA concentration and purity were assessed by NanoDrop One (Thermo Fisher, USA). One microgram of total RNA was reverse transcribed into cDNA using the RevertAid First Strand cDNA Synthesis Kit (3328929, Thermo, USA). The qRT-PCR was performed on a QuantStudio 5 Real-Time PCR System (Applied Biosystems, USA) with the following thermal cycling profile: 95°C for 30s, followed by 40 cycles of 95°C for 5s and 60°C for 30s. The primer sequences used were:PTTG1forward 5'- GCCTCTCATGATCCTTGACG-3', reverse 5'-AAGGGCACTTGCTCACTTAC-3'; β -actin forward 5'-GCGAGCATCCCCCAAAGTTC-3', reverse 5'-AGTGGGGTGGCTTTTAGGATG-3'. Each reaction was performed in technical triplicate. Melt curve analysis confirmed single-product amplification. PTTG1 mRNA expression in tumor tissue was calculated relative to its matched adjacent normal tissue using the $2^{-\Delta\Delta Ct}$ method, with β -actin as the internal reference.

Immunohistochemistry (IHC)

Formalin-fixed paraffin-embedded (FFPE) tissue sections (4 μm) from five paired UCEC tumors and adjacent normal endometrial tissues were deparaffinized in xylene, rehydrated through graded ethanol, and subjected to heat-induced antigen retrieval in citrate buffer (pH 6.0). Endogenous peroxidase activity was blocked with 3% H_2O_2 for 15 minutes. Sections were incubated with anti-PTTG1 primary antibody (rabbit monoclonal, 1:200 dilution, Proteintech, 18040-1-AP, China) overnight at 4°C, followed by HRP-conjugated goat anti-rabbit secondary antibody (ab6721, Abcam) incubation at room temperature for 30 minutes. DAB chromogen (Dako) was used for visualization, and sections were counterstained with hematoxylin. Staining intensity and distribution were evaluated under light microscopy. A representative pair of tumors and adjacent normal sections were selected for presentation.

CPTAC Proteomic Analysis

PTTG1 protein expression data in UCEC were obtained from the Clinical Proteomic Tumor Analysis Consortium (CPTAC) via two independent sources. (1) Tumor versus normal protein Z-score comparison was retrieved from UALCAN (http://ualcan.path.uab.edu/), which provides precomputed CPTAC proteomic data for 31 normal endometrial and 100 primary UCEC tumor samples. (2) Paired mRNA and protein abundance data for PTTG1 (n = 42 samples with matched proteomic and transcriptomic profiles) were downloaded from the CPTAC-UCEC 2020 study deposited in cBioPortal (https://www.cbioportal.org/study/summary?id=ucec_cptac_2020). For the mRNA-protein correlation analysis, RNA-Seq values ($\log_2$ RSEM) and protein abundance values ($\log_2$ ratio) were extracted, and the Pearson correlation coefficient was computed. Statistical significance of the tumor versus normal comparison was assessed by the Mann-Whitney U test.

Statistical Analysis

All statistical analyses and data visualizations in this study were permanently executed using R software (version 4.4.3). Continuous variables between two independent groups were compared using the non-parametric Wilcoxon rank-sum test. For multi-group comparisons of continuous variables, the Kruskal-Wallis test was employed, followed by pairwise post-hoc comparisons where appropriate. The correlation between continuous variables (such as gene co-expression networks and immune cell infiltration abundances) was evaluated using the Spearman correlation coefficient (r). The diagnostic efficacy of the identified hub genes was quantified by establishing ROC curves and calculating the AUC along with 95% CIs. For prognostic evaluation, K-M survival curves for both OS and PFI were generated using the TCGA-UCEC clinical annotation. Patients were stratified into high- and low-expression groups based on the median PTTG1 mRNA expression level, and statistical significance was evaluated using the log-rank test. Hazard Ratios HR and 95% CIs were computed via the Cox proportional hazards model. Variables contributing to patient survival were further examined using univariate and multivariate Cox proportional hazards regression models to calculate HR and corresponding 95% CIs. All statistical tests performed were two-tailed, and a p-value < 0.05 (or adjusted p-value < 0.05 for multiple testing corrections, such as Benjamini-Hochberg False Discovery Rate) was considered statistically significant. All experimental data were presented as mean ± standard deviation (SD) from at least three

independent experiments. The paired Student's t-test was used to compare PTTG1 expression between tumor and matched normal tissues at both the protein (WB densitometry) and mRNA (qRT-PCR) levels. Pearson correlation coefficient was used to evaluate the association between tissue qRT-PCR fold change and WB densitometry ratios (mRNA-protein concordance). A p-value < 0.05 was considered statistically significant, statistical analyses and graphing were performed using GraphPad Prism 9.0 (GraphPad Software, USA).

Results

Differential Expressing Analysis

To identify robust transcriptomic alterations associated with UCEC, we systematically integrated three independent GEO microarray datasets (GSE17025, GSE115810, and GSE63678). Given the inherent technical biases across different platforms, the ComBat algorithm was applied to remove batch effects. PCA revealed that prior to correction, samples clustered predominantly by their dataset of origin (Fig. 1A, left). Following correction, the dataset-specific clustering was eliminated, and samples from all three cohorts were uniformly mixed while maintaining a distinct separation between normal and cancer groups (Fig. 1A, right). Box plots further confirmed the efficacy of normalization, demonstrating that the disparate expression distributions were successfully aligned across all samples (Fig. 1B). Based on the batch-corrected integrated dataset, differential expression analysis was performed using the limma package. With the cutoff criteria of $|logFC| > 1$ and adjusted p -value < 0.05, a total of 531 DEGs were identified, comprising 254 significantly upregulated and 277 downregulated genes in UCEC tissues compared to normal tissues (Fig. 1C). Hierarchical clustering of the top 50 DEGs visualized in a heatmap exhibited highly consistent intragroup expression patterns and stark contrasts between cancer and normal samples (Fig. 1D).

To uncover the biological implications of the identified DEGs, GO and KEGG enrichment analyses were conducted. KEGG pathway analysis indicated significant enrichment in the Cell cycle, IL-17 signaling pathway, Apoptosis, and Chemokine signaling pathways (Fig. 1E). Consistently, GO analysis revealed that these DEGs were primarily enriched in cell cycle-related biological processes, such as mitotic sister chromatid segregation and nuclear division. Cellular components were enriched in spindle and kinetochore, while molecular functions were associated with microtubule binding and tubulin binding (Fig. 1F). These findings suggest that the DEGs play pivotal roles in tumor proliferation and the immune microenvironment in UCEC.

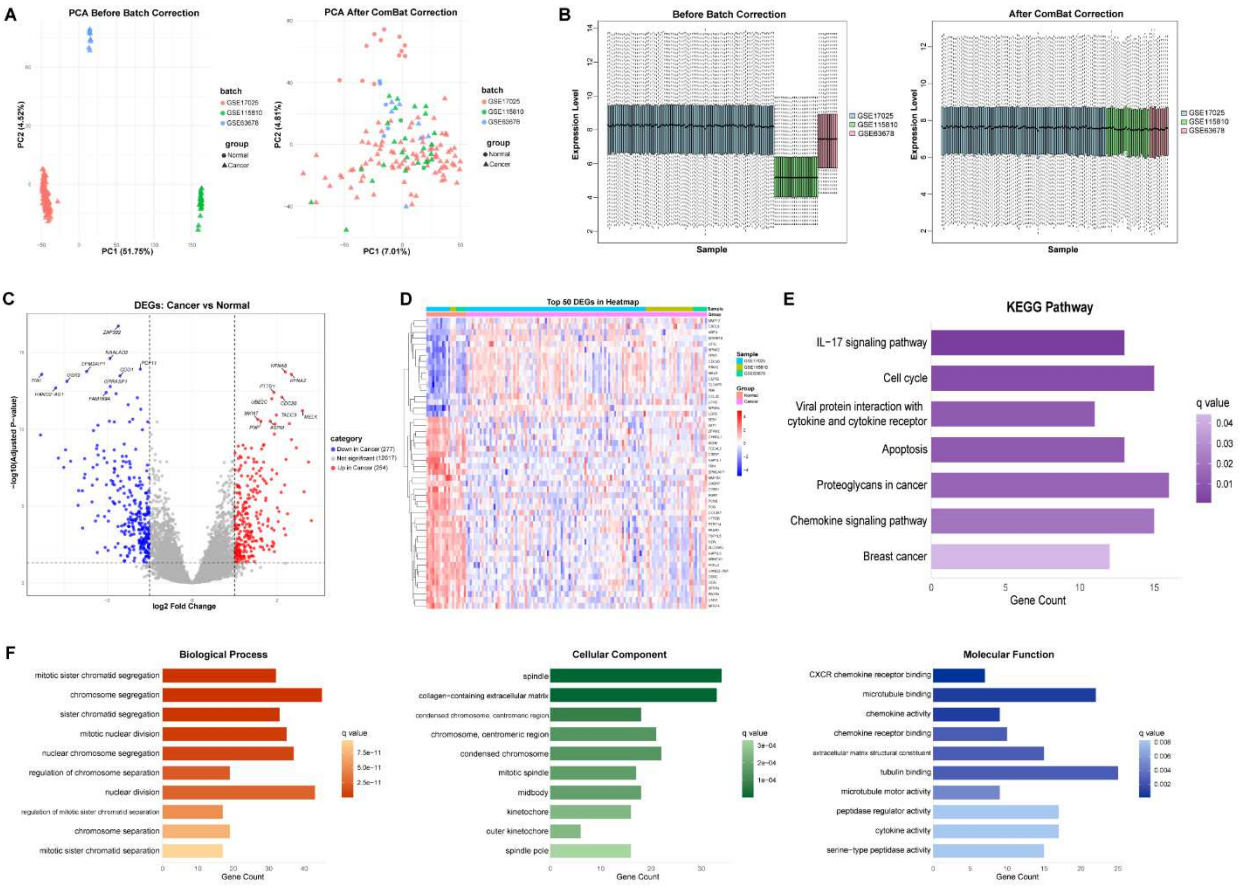


Figure 1. Data integration, identification of differentially expressed genes (DEGs), and functional enrichment analysis in endometrial cancer. (**A**) Principal component analysis (PCA) plots of the merged GEO datasets before (left) and after (right) ComBat batch effect correction. Colors represent different GEO cohorts, and shapes indicate sample groups (Normal vs. Cancer). (**B**) Box plots illustrating the gene expression distributions across all samples before (left) and after (right) batch effect correction. (**C**) Volcano plot showing DEGs between cancer and normal tissues in the integrated dataset. Red and blue dots denote significantly upregulated (n = 254) and downregulated (n = 277) genes, respectively (|logFC| > 1 and adjusted $p < 0.05$). (**D**) Hierarchical clustering heatmap of the top 50 DEGs, displaying distinct expression patterns between cancer and normal groups. (**E**) Kyoto Encyclopedia of Genes and Genomes (KEGG) pathway enrichment analysis of the DEGs. (**F**) Gene Ontology (GO) enrichment analysis of the DEGs across biological processes, cellular components, and molecular functions.

Identification of Hub Genes via WGCNA

To systematically identify highly coordinated gene modules associated with UCEC, WGCNA was performed on the integrated GEO dataset. To ensure a scale-free network topology, an optimal soft-thresholding power of β=5 was selected (Fig. 2A, B). Through hierarchical clustering and dynamic tree cutting, genes were assigned into distinct co-expression modules, which are represented by different colors under the gene dendrogram (Fig. 2C, Supplementary Fig.1A). Subsequently, module-trait relationship analysis was conducted to correlate these modules with the tissue type. As shown in the heatmap, several modules were significantly correlated with UCEC (Fig. 2D). Notably, the turquoise and yellow modules exhibited highly significant positive correlations with the cancer phenotype (Fig. 2E, F), while the blue module showed a strong negative correlation (Supplementary Fig.1B). Scatter plots of Gene Significance (GS) versus Module Membership (MM) further demonstrated a highly significant positive correlation within these key modules,

indicating that genes within these modules play a crucial role in UCEC progression. Therefore, genes from the most significantly cancer-associated modules were extracted as tumor-related module genes for downstream analysis.

To pinpoint the most robust genes driving UCEC development, we intersected the cancer-related module genes identified via WGCNA (n = 100) with the previously identified DEGs (n = 531). As illustrated in the Venn diagram, a total of 65 consensus candidate genes were identified in the intersection (Fig. 2G). To explore the biological significance of these 65 candidate genes, GO and KEGG enrichment analyses were performed. GO analysis indicated that these genes are highly enriched in cell cycle-related functions, including mitotic sister chromatid segregation, spindle organization, and microtubule binding (Fig. 2H). Consistently, KEGG pathway analysis highlighted their involvement in critical oncogenic and immune-related signaling pathways, such as Apoptosis, Cell cycle, and the IL-17 signaling pathway (Fig. 2I). These 65 genes were thus selected as the core candidate pool for subsequent machine learning screening.

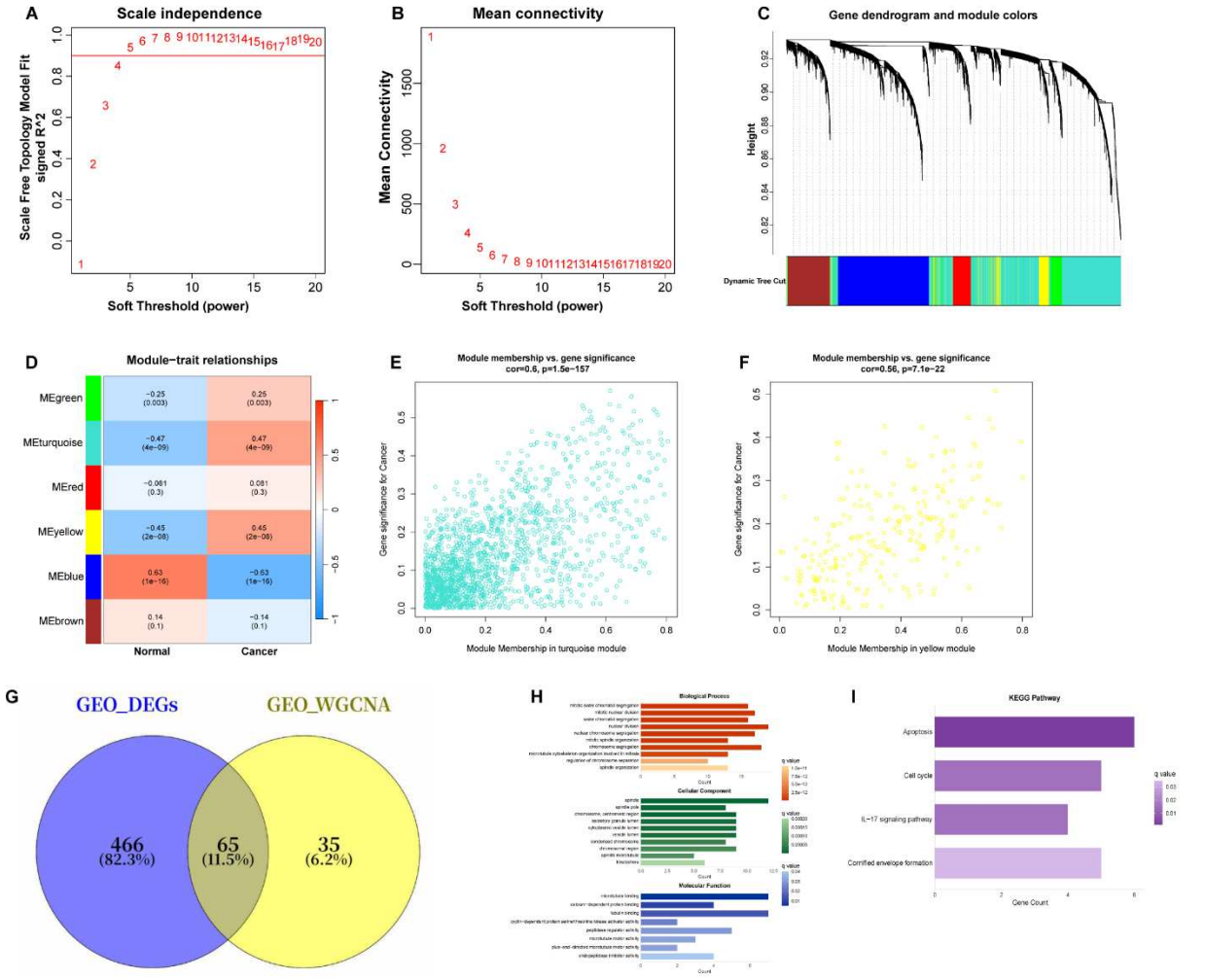


Figure 2. Weighted gene co-expression network analysis (WGCNA) and identification of consensus candidate genes in UCEC. (**A**) Analysis of the scale-free fit index (scale independence) for various soft-thresholding powers. (**B**) Analysis of the mean connectivity for various soft-thresholding powers. (**C**) Gene dendrogram and module colors generated by hierarchical clustering, with branches representing individual genes and colors representing co-expression modules. (**D**) Heatmap of module-trait relationships evaluating the correlation between module eigengenes and clinical status (Normal vs. Cancer). (**E-F**) Scatter plots of gene significance (GS) for cancer versus module membership (MM) in the key tumor-related modules (e.g., turquoise and yellow modules). (**G**) Venn diagram illustrating the intersection between differentially expressed genes (GEO_DEGs) and key WGCNA module genes (GEO_WGCNA), yielding 65 consensus candidate genes. (**H**) GO enrichment analysis of the 65 consensus genes across biological processes (BP), cellular components (CC), and molecular functions (MF). (**I**) KEGG pathway enrichment analysis of the 65 consensus genes.

Screening of Core Genes Using Machine Learning Algorithms

To further narrow down the 65 consensus candidate genes and identify the most robust diagnostic biomarkers for UCEC, a comprehensive screening framework integrating four complementary machine learning algorithms was utilized: LASSO, SVM-RFE, XGBoost, and Boruta. First, LASSO logistic regression with 5-fold cross-validation was applied to penalize less informative features, selecting a robust subset of genes based on the optimal lambda value (Fig. 3A, B). Concurrently, the SVM-RFE algorithm was employed to recursively eliminate features and determine the optimal subset that maximized the classification performance. The model achieved a peak cross-

validation accuracy of 0.9089 and a minimum error of 0.0911 when the feature number was narrowed to 25 (Fig. 3C, D). Next, the XGBoost algorithm evaluated feature importance based on predictive Gain and SHAP values. The SHAP summary plot and Gain ranking prominently highlighted genes such as CDC20, PTTG1, and PNP as the top contributors to the model's predictive capability (Fig. 3E, F). Furthermore, the Boruta algorithm iteratively compared original attributes with randomized shadow features, confirming a subset of robust genes with significantly higher Z-scores than the maximum Z-score of shadow features (Fig. 3G, H). Finally, to ensure the highest reliability and generalizability of the biomarkers, the overlapping genes identified by all four machine learning algorithms were extracted. As shown in the Venn diagram, exactly 5 consensus core genes—PNP, CDC20, PTTG1, S100A11, and KLF5—were successfully identified at the intersection (Fig. 3I). These 5 core genes were thus advanced for downstream independent clinical validation.

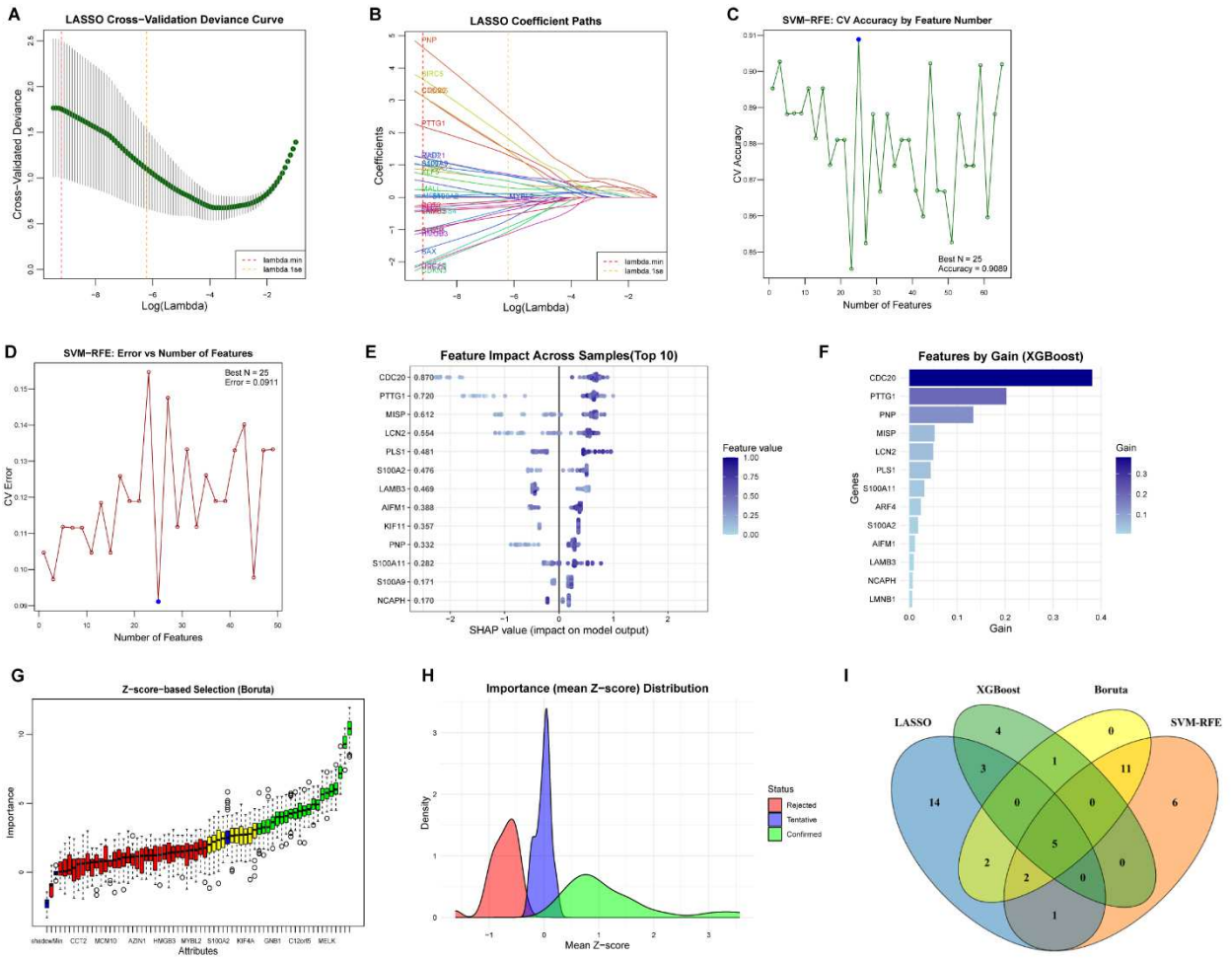


Figure 3. Machine learning-based screening of core diagnostic genes from the 65 consensus candidate genes. (**A, B**) LASSO logistic regression analysis. (**A**) Ten-fold cross-validation deviance curve for selecting the optimal penalty parameter (lambda). (**B**) LASSO coefficient paths of the candidate genes at varying lambda values. (**C, D**) Support Vector Machine-Recursive Feature Elimination (SVM-RFE) algorithm. (**C**) Cross-validation accuracy curve peaking at 25 features. (**D**) Cross-validation error curve reaching the minimum at 25 features. (**E, F**) Extreme Gradient Boosting (XGBoost) feature importance analysis. (**E**) SHAP (SHapley Additive exPlanations) summary plot demonstrating the impact of the top features on the model output. (**F**) Bar plot showing the top features ranked by predictive Gain. (**G, H**) Boruta algorithm feature selection.(**G**) Boxplots of Z-scores for confirmed (green), tentative (blue/yellow), and rejected (red) features compared to shadow features. (**H**) Density distribution of the mean Z-scores for the different feature categories. (**I**) Venn diagram illustrating the intersection of key features selected by the LASSO, SVM-RFE, XGBoost, and Boruta algorithms, identifying 5 consensus core genes.

Validation, Diagnostic Value, and Prognostic Significance of Core Genes

To evaluate the clinical applicability of the machine learning-derived core genes (PNP, CDC20, PTTG1, S100A11, and KLF5), we first verified their expression profiles. As depicted in Fig. 4A, all five genes were significantly upregulated in UCEC tissues compared to normal tissues (all $p < 0.001$), consistent with our initial differential expression analysis. Next, ROC curves were generated to assess their diagnostic performance in distinguishing UCEC from normal samples. All five genes demonstrated strong diagnostic efficacy, with CDC20 (AUC = 0.983; 95% CI: 0.961–1.000) and PTTG1 (AUC = 0.971; 95% CI: 0.938–1.000) displaying exceptional sensitivity and specificity (Fig. 4B).

To further screen for genes with crucial prognostic value, we performed Kaplan-Meier survival analyses utilizing the TCGA-UCEC clinical cohort. Patients were stratified into high and low expression groups based on median gene expression levels. Remarkably, while all five genes possessed high diagnostic value, only the overexpression of PTTG1 was significantly associated with a poorer OS in UCEC patients ($p = 0.002$, Hazard Ratio = 1.93, 95% CI: 1.27–2.93) (Fig. 4E). The expression levels of PNP, CDC20, S100A11, and KLF5 did not show significant correlations with patient overall survival (all $p > 0.05$, Fig. 4C, 4D, 4F, 4G). Considering that overall survival in UCEC patients may be confounded by non-tumor-related mortality, particularly in the typically elderly female population, we extended our prognostic analysis to the PFI, a more disease-specific endpoint that captures tumor recurrence and progression events. In line with the OS findings, patients in the PTTG1-high group experienced a markedly worse PFI compared with the PTTG1-low group, with a Hazard Ratio of 2.10 (95% CI: 1.46–3.02, $p < 0.001$) (Fig. 4H). The convergence of the OS and PFI analyses—the latter reflecting an even more pronounced hazard than OS—further substantiates the prognostic robustness of PTTG1 and underscores its potential to predict not only cancer-related mortality but also early disease progression in UCEC. Consistent with these findings, paired differential expression analysis of the 23 matched tumor-normal pairs from the TCGA-UCEC cohort confirmed that PTTG1, PNP, and CDC20 were robustly upregulated in tumor tissues (all $p < 0.0001$), while S100A11 was moderately upregulated ($p < 0.001$) and KLF5 showed no significant difference (Supplementary Fig. 2A–E). Given the lack of significant OS associations for the four non-PTTG1 core genes, we further interrogated their prognostic value using progression-free interval (PFI) as a more disease-specific endpoint. Among these, only CDC20 exhibited a statistically significant association with worse PFI ($p = 0.003$; Supplementary Fig. 2G), whereas PNP ($p = 0.350$), S100A11 ($p = 0.279$), and KLF5 ($p = 0.463$) showed no significant prognostic value (Supplementary Fig. 2F, H, I). Consequently, PTTG1 stood out as the most robust and clinically relevant biomarker, prompting us to focus our subsequent multi-dimensional analyses exclusively on PTTG1.

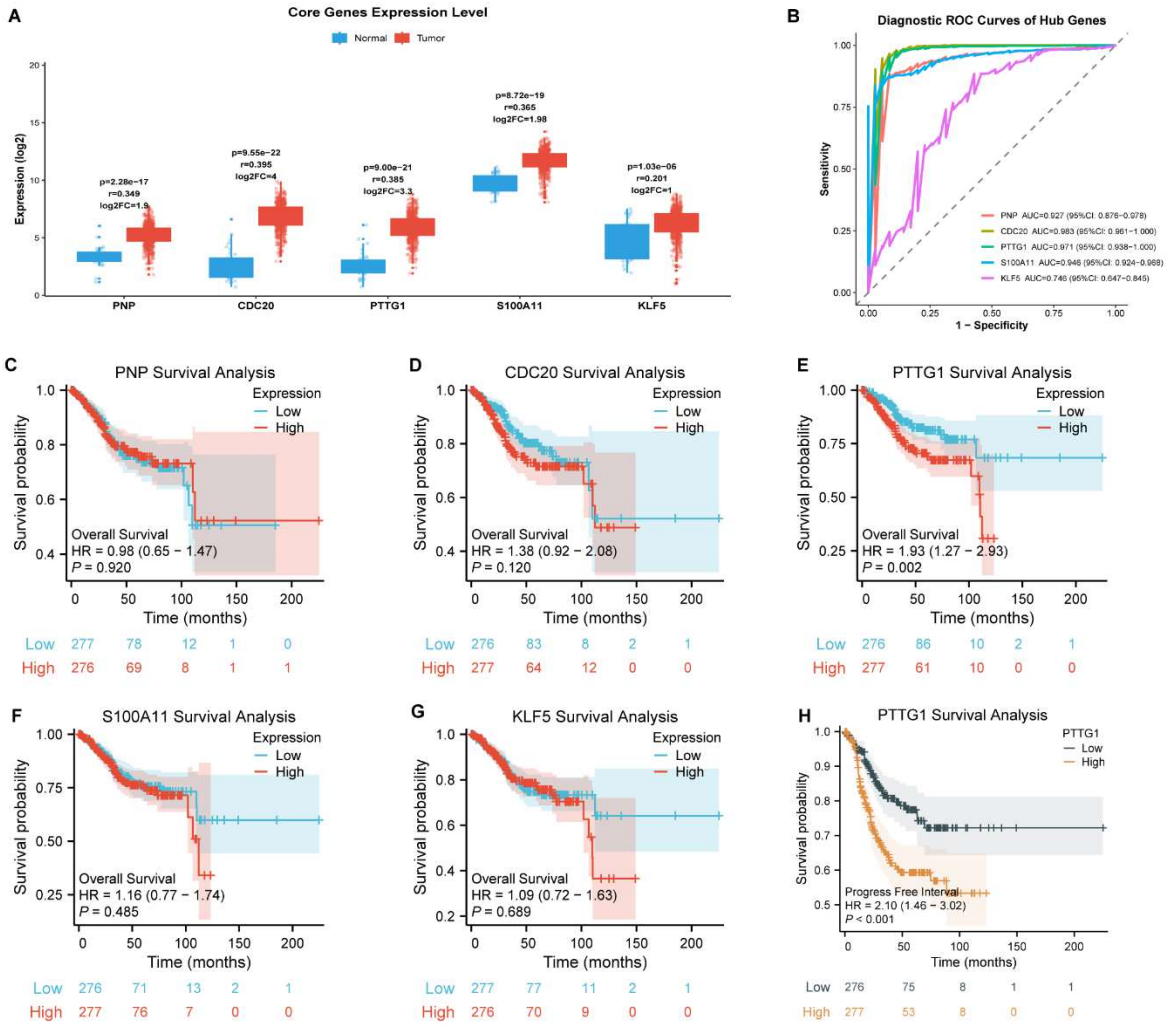


Figure 4. **Expression validation, diagnostic efficacy, and prognostic significance of the five consensus core genes in UCEC**. (**A**) Boxplots illustrating the significant upregulation of the five core genes (PNP, CDC20, PTTG1, S100A11, and KLF5) in tumor tissues compared to normal tissues. p-values and log2 fold-changes are indicated above each gene. (**B**) Receiver Operating Characteristic (ROC) curves evaluating the diagnostic accuracy of the five hub genes. The Area Under the Curve (AUC) values are provided, demonstrating excellent diagnostic performance, particularly for CDC20 (AUC = 0.983) and PTTG1 (AUC = 0.971). (**C–G**) Kaplan-Meier overall survival (OS) analysis for UCEC patients stratified by high and low expression levels of (**C**) PNP, (D) CDC20, (E) PTTG1, (F) S100A11, and (**G**) KLF5. Only PTTG1 exhibited a statistically significant association with overall survival (p = 0.002, Hazard Ratio = 1.93), establishing it as an independent prognostic biomarker.(**H**) Progression-free interval (PFI) analysis of PTTG1 in the TCGA-UCEC cohort. High PTTG1 expression was significantly associated with a markedly worse PFI (HR = 2.10, 95% CI: 1.46–3.02, p < 0.001), further validating the prognostic value of PTTG1 from a disease-progression-oriented perspective and establishing it as an independent prognostic biomarker for both overall survival and tumor progression in UCEC.

Correlation of PTTG1 Expression with Clinicopathological Features

Given the robust prognostic value of PTTG1, we further investigated its relationship with various clinicopathological characteristics in the TCGA-UCEC cohort. A comprehensive heatmap visually demonstrated that high PTTG1 expression was significantly enriched in patients with advanced tumor stages, higher histological grades, and specific histological types (Fig. 5A). Detailed quantitative analyses using violin plots further substantiated these findings. PTTG1 expression was

significantly elevated in older patients (> 65 years, $p = 0.024$, Fig. 5B) and showed striking disparities across histological subtypes, with the highly aggressive Serous carcinoma exhibiting significantly higher PTTG1 levels compared to Endometrioid carcinoma ($p = 1.2e-05$, Fig. 5D). Importantly, PTTG1 expression increased stepwise with disease progression; its expression was remarkably higher in advanced tumor stages (Stage III/IV) compared to early stages (Stage I/II) ($p = 3.9e-05$, Fig. 5E, F). Furthermore, a highly significant positive correlation was observed between PTTG1 expression and histological grade, peaking in poorly differentiated G3 tumors ($p < 2e-16$, Fig. 5G). No significant correlations were observed between PTTG1 expression and overall survival status at baseline without time-to-event adjustment ($p = 0.1$, Fig. 5C). Although PTTG1 expression did not differ significantly across BMI categories overall ($p = 0.061$, Fig. 5H), comparison revealed significantly elevated PTTG1 expression in obese patients compared with normal weight patients ($p < 0.05$). Collectively, these clinicopathological correlations strongly indicate that elevated PTTG1 expression is intricately associated with aggressive tumor phenotypes, advanced clinical stages, and poor differentiation in UCEC, underscoring its potential role as a driver of malignant progression.

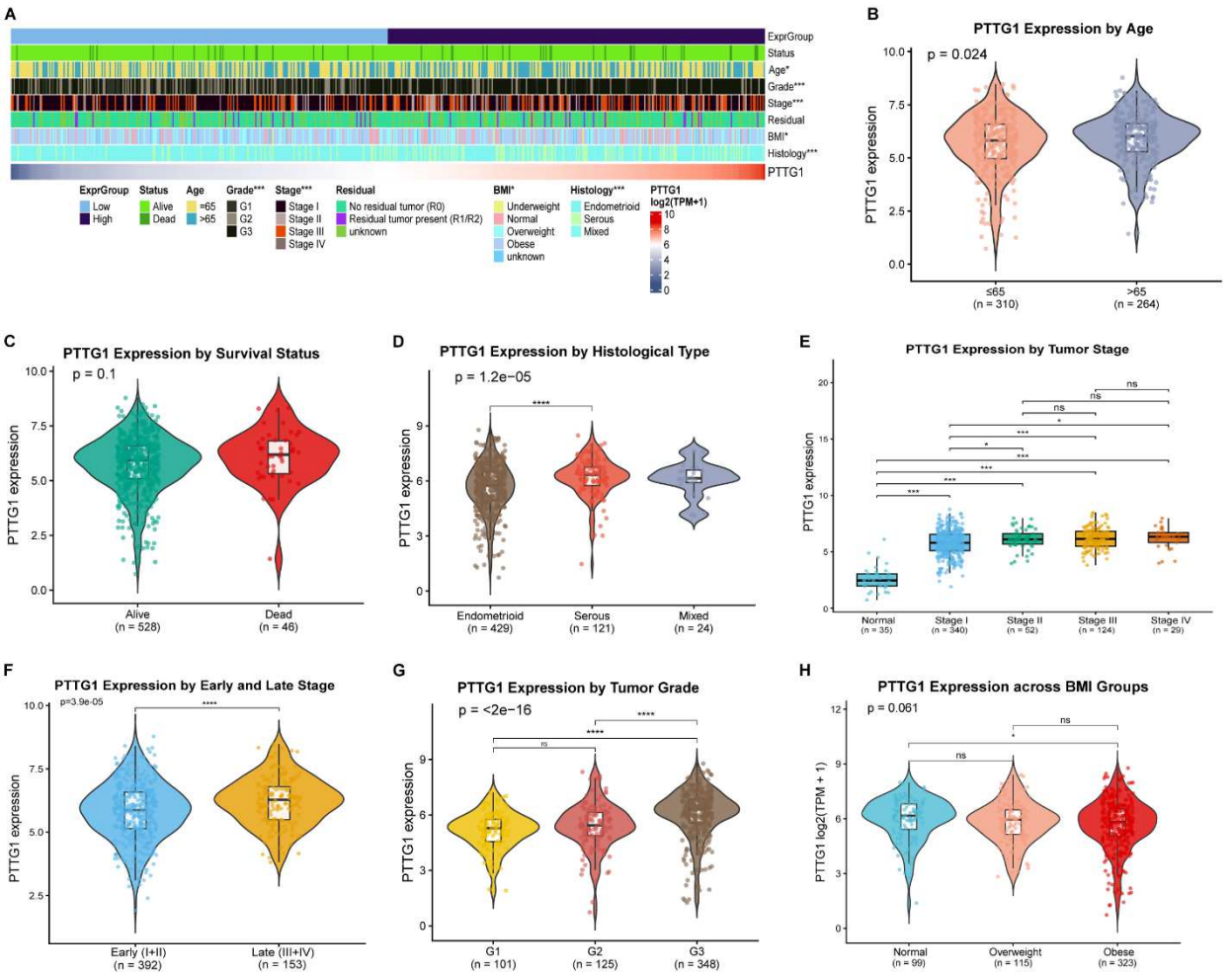


Figure 5. Association between PTTG1 expression and clinicopathological characteristics in the TCGA-UCEC cohort. (**A**) Comprehensive heatmap illustrating the distribution of clinicopathological features (Age, Grade, Stage, Residual tumor, BMI, and Histology) ranked by PTTG1 expression levels (Low vs. High). Asterisks denote statistical significance. (**B–H**) Violin plots evaluating the differential expression of PTTG1 stratified by (**B**) Age (≤65 vs. > 65), (**C**) Survival Status (Alive vs. Dead), (**D**) Histological Type (Endometrioid, Serous, and Mixed), (**E**) Tumor Stage (Normal, Stage I, II, III, and IV), (**F**) Early (I+II) versus Late (III+IV) Stage, (**G**) Tumor Grade (G1, G2, and G3), and (**H**) Body Mass Index (BMI). P-values were calculated to determine statistical significance. Asterisks denote the level of statistical significance (* p≤0.05, ** p≤0.01, *** p≤0.001, **** p≤0.0001; ns, not significant).

Co-expression Network and Biological Functions of PTTG1 in UCEC

To elucidate the potential molecular mechanisms by which PTTG1 drives UCEC progression, we constructed a co-expression network based on the TCGA-UCEC transcriptomic data. Genes significantly correlated with PTTG1 were screened using Spearman correlation analysis (threshold: $r > 0.4$ and $p < 0.001$). Our analysis identified a robust cluster of genes tightly co-expressed with PTTG1. Notably, the top three genes exhibiting the strongest positive correlations with PTTG1 were CDC25C ($r = 0.858$), UBE2C ($r = 0.881$), and CDCA3 ($r = 0.850$) (Fig. 6A–C), all of which are well-documented critical regulators of the cell cycle and mitosis. Conversely, genes such as FAM189A2, FCER1A, and IGFBP4 exhibited the strongest negative correlations with PTTG1 expression (Fig. 6D–F). To further decipher the biological implications of this PTTG1-driven network, we performed GO and KEGG pathway enrichment analyses on the significantly correlated genes. GO analysis vividly demonstrated that these co-expressed genes are predominantly

enriched in mitosis-related and chromosome segregation processes, including nuclear division, condensed chromosome, spindle organization, and microtubule binding (Fig. 6G). Consistently, KEGG pathway analysis highlighted a massive enrichment in the Cell cycle pathway, along with other critical cellular processes such as DNA replication and Homologous recombination (Fig. 6H). To further dissect the pathway-level implications of PTTG1 expression, GSEA was performed. In the PTTG1-high expression group, five hallmark pathways—cell cycle, DNA replication, mismatch repair, proteasome, and spliceosome—were significantly activated (Supplementary Fig. 1C). Conversely, the PTTG1-low expression group exhibited enrichment in immune-related pathways, including complement and coagulation cascades, cytokine-cytokine receptor interaction, graft-versus-host disease, hematopoietic cell lineage, and intestinal immune network for IgA production (Supplementary Fig. 1E). These bidirectional GSEA findings corroborate the dual intrinsic proliferative and extrinsic immune-modulatory roles of PTTG1.Collectively, these robust bioinformatics findings strongly imply that PTTG1 acts as a pivotal oncogene in UCEC by orchestrating a complex network of cell cycle regulators, thereby continuously promoting uncontrolled tumor cell proliferation and division.

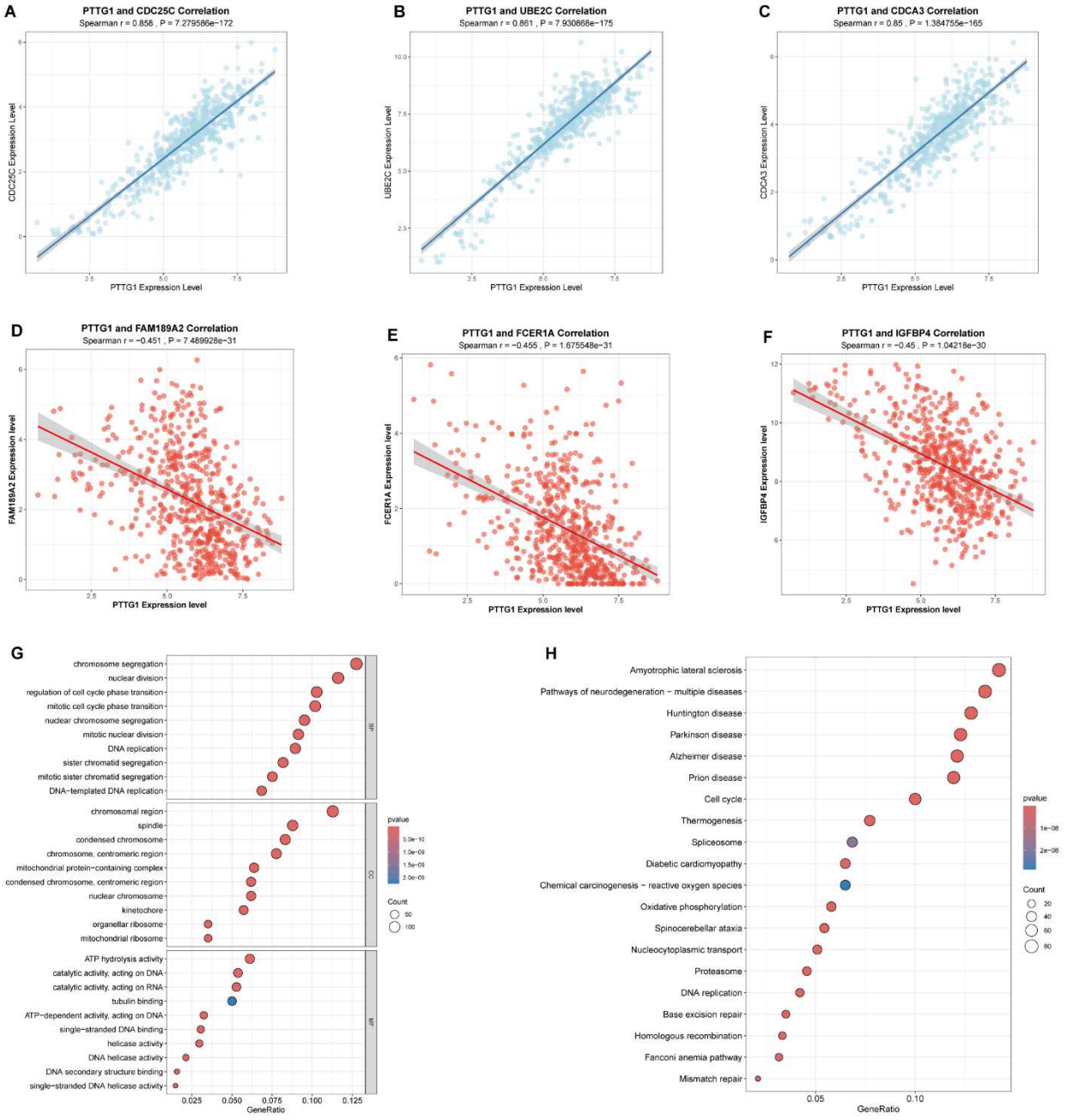


Figure 6. Co-expression network and functional enrichment analysis of PTTG1 in UCEC. (**A–C**) Scatter plots with linear regression lines demonstrating the top three genes most significantly positively correlated with PTTG1 expression in the TCGA-UCEC cohort: (**A**) CDC25C, (**B**) UBE2C, and (**C**) CDCA3. (**D–F**) Scatter plots demonstrating the top three genes most significantly negatively correlated with PTTG1 expression: (**D**) FAM189A2, (**E**) FCER1A, and (**F**) IGFBP4. Spearman correlation coefficients (r) and P-values are displayed at the top of each plot. (**G**) Bubble plot of GO enrichment analysis for the PTTG1-correlated gene network, categorized by biological processes, cellular components, and molecular functions. (**H**) Bubble plot of KEGG pathway enrichment analysis for the PTTG1-correlated genes.

PTTG1 Reshapes the Tumor Immune Microenvironment

Given the pivotal role of TIME in tumor progression and therapy resistance, we comprehensively investigated the impact of PTTG1 expression on the UCEC microenvironment. First, the CIBERSORT algorithm was utilized to evaluate the relative infiltration fractions of 22 immune cell subpopulations. Significant differences in immune cell composition were observed between the PTTG1-High and PTTG1-Low groups (Fig. 7A). To further quantify these relationships, global Spearman correlation analysis was performed (Fig. 7B). Specifically, PTTG1 expression was significantly and positively correlated with the proportions of T cells follicular helper ($r = 0.26$), T cells CD4 memory activated ($r = 0.20$), and Macrophages M1 ($r = 0.18$). Conversely, it exhibited strong negative correlations with T cells regulatory (Tregs) ($r = -0.33$), Dendritic cells resting ($r = -0.20$), and T cells CD4 memory resting ($r = -0.14$) (Fig. 7C). These findings suggest that PTTG1 critically alters the microscopic composition of infiltrating immune cells. To comprehensively map the immune-associative landscape of the machine-learning-derived core genes, Spearman correlation analysis was performed between the five core genes (PTTG1, PNP, CDC20, S100A11, and KLF5) and 22 infiltrating immune cell subtypes. PTTG1 exhibited significant positive correlations with multiple immunosuppressive and effector cell populations (Supplementary Fig. 1D).

While CIBERSORT evaluates the relative proportions of immune cells, we subsequently applied the ESTIMATE algorithm to assess the absolute macroscopic TME scores. Strikingly, patients in the PTTG1-High group exhibited drastically lower StromalScores and ImmuneScores compared to the PTTG1-Low group (all $p \leqslant 0.0001$, Fig. 7D). Consequently, the overall ESTIMATEScore was highly significantly decreased in the PTTG1-High cohort ($p \leqslant 0.0001$). Since a lower ESTIMATEScore is mathematically indicative of a higher tumor purity, these compelling macro-level results strongly suggest that PTTG1 overexpression drives the formation of a highly pure, cold tumor microenvironment. The severe overall depletion of stromal and immune cell infiltration, combined with the altered microscopic immune composition, may facilitate immune evasion and contribute to the highly aggressive phenotype observed in PTTG1-high UCEC patients.

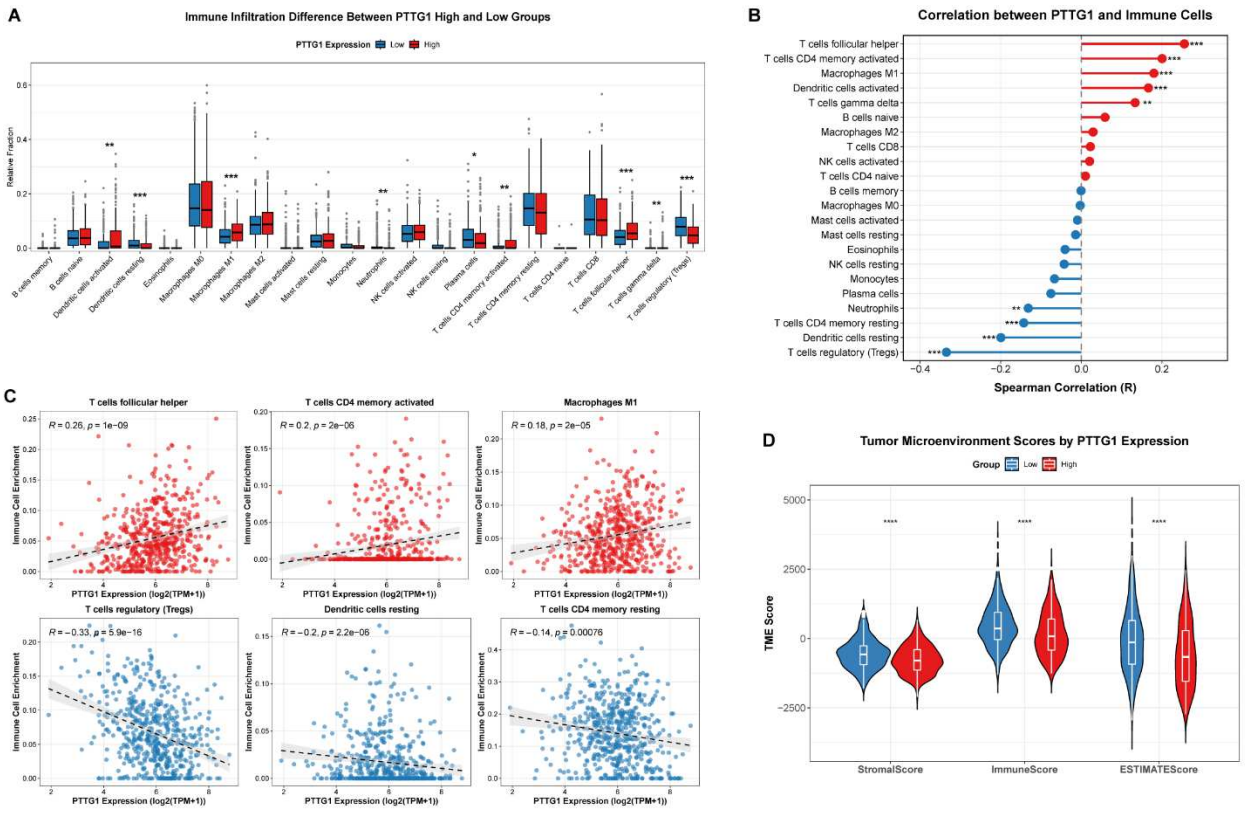


Figure 7. Macroscopic and microscopic landscape of the tumor immune microenvironment (TME) regulated by PTTG1 in UCEC. (**A**) Boxplots comparing the relative fractions of 22 immune cell types between the PTTG1-High and PTTG1-Low expression groups. (**B**) Lollipop plot illustrating the global Spearman correlations between continuous PTTG1 expression and the infiltration levels of the 22 immune cell subpopulations. Red lines indicate positive correlations, while blue lines indicate negative correlations. (**C**) Representative scatter plots depicting the most significant positive (top row: T cells follicular helper, T cells CD4 memory activated, and Macrophages M1) and negative (bottom row: T cells regulatory [Tregs], Dendritic cells resting, and T cells CD4 memory resting) correlations between PTTG1 expression and specific immune cells. (**D**) Violin plots comparing the macroscopic TME profiles, including StromalScore, ImmuneScore, and ESTIMATEScore, between the PTTG1-High and PTTG1-Low groups. Asterisks denote the level of statistical significance (* p≤0.05, **p≤0.01, *** p≤0.001, **** p≤ 0.0001; Wilcoxon rank-sum test or Spearman correlation test).

Drug Sensitivity Prediction for Personalized Therapy Guided by PTTG1

Given the poor prognosis and the highly immunosuppressive tumor microenvironment associated with PTTG1 overexpression, it is imperative to explore alternative targeted therapies or chemotherapeutic strategies for these high-risk UCEC patients. Using the oncoPredict algorithm based on large-scale pharmacogenomics databases, we comprehensively evaluated the sensitivities of UCEC patients to various anti-cancer drugs. Our global screening revealed extensive and highly significant differences in drug sensitivities between the PTTG1-High and PTTG1-Low groups (Fig. 8A). To pinpoint the most clinically relevant agents, we calculated the median sensitivity differences and ranked the top 10 drugs most effective for each group (Fig. 8B). Notably, patients in the PTTG1-High group exhibited significantly higher predicted sensitivities to specific targeted therapies, including the MEK inhibitors Selumetinib and Trametinib, as well as the MDM2 inhibitor Nutlin-3a (-) (all $p < 0.0001$) (Fig. 8C–E). Spearman correlation analysis further confirmed a robust positive correlation between PTTG1 expression levels and the predicted sensitivity to

Selumetinib (r = 0.46, p < 2.2e-16) (Fig. 8F). Conversely, patients with high PTTG1 expression demonstrated remarkable resistance to another subset of drugs, including AZD5991, P22077, and WEHI-539 (all p < 0.0001) (Fig. 8G–I). Continuous expression profiling verified a significant negative correlation between PTTG1 expression and the sensitivity to AZD5991 (r = -0.22, p = 2.4e-07) (Fig. 8J). Collectively, these robust pharmacogenomic predictions indicate that PTTG1 is not merely a prognostic biomarker but also a critical predictive indicator for drug response. For high-risk, PTTG1-overexpressing UCEC patients who may not benefit from conventional immunotherapies, targeted interventions utilizing MEK or MDM2 inhibitors could represent a highly promising and personalized therapeutic strategy.

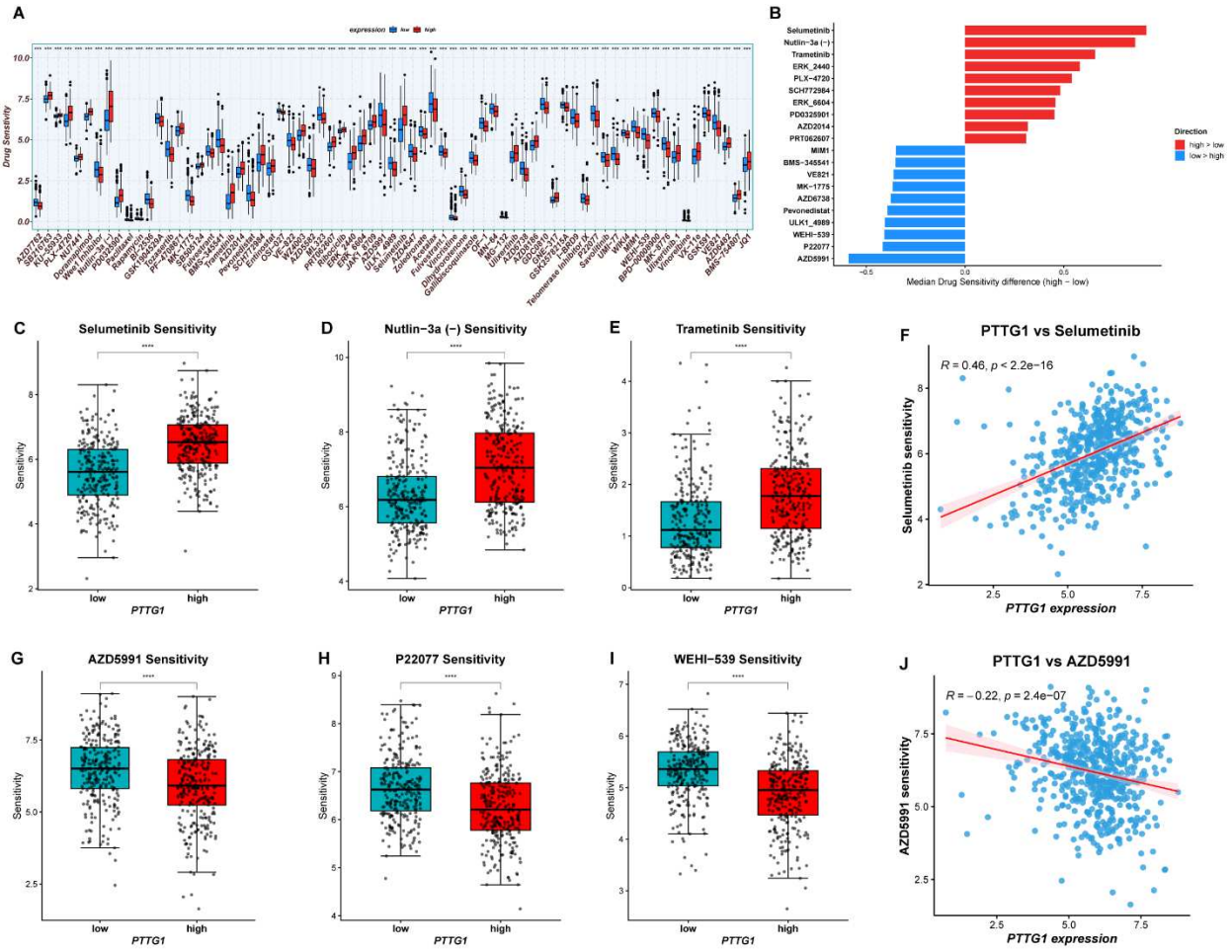


Figure 8. **Prediction of targeted therapy and chemotherapeutic drug sensitivity based on PTTG1 expression in UCEC**. (**A**) Boxplots comparing the overall predicted drug sensitivities (IC50 or sensitivity scores) of multiple therapeutic agents between the PTTG1-High and PTTG1-Low groups. (**B**) Bar plot illustrating the top 10 drugs with higher sensitivity in the PTTG1-High group (red bars) and the top 10 drugs with higher sensitivity in the PTTG1-Low group (blue bars), calculated by the median sensitivity difference. (**C–E**) Representative boxplots detailing the predicted sensitivities of specific drugs, including (**C**) Selumetinib, (**D**) Nutlin-3a (-), and (**E**) Trametinib, between the high and low PTTG1 groups. (**F**) Scatter plot revealing a significant positive correlation between continuous PTTG1 expression and Selumetinib sensitivity (Spearman r = 0.46, p < 2.2e-16). (**G–I**) Representative boxplots detailing the predicted sensitivities of drugs with opposite efficacy profiles, including (**G**) AZD5991, (H) P22077, and (**I**) WEHI-539. (**J**) Scatter plot illustrating a significant negative correlation between PTTG1 expression and AZD5991 sensitivity (Spearman r = -0.22, p = 2.4e-07). Asterisks denote the significance levels (* p≤0.05, ** p≤0.01, *** p≤0.001).

Single-Cell and Spatial Transcriptomic Characterization of PTTG1

To dissect the precise cellular origins and anatomical distribution of PTTG1 at unprecedented resolution, we integrated scRNA-seq with ST data from UCEC. Following stringent quality control, unsupervised clustering mapped the single cells into 21 distinct clusters (Fig. 9A, Supplementary Fig. 3A, 3B), The top 3,000 highly variable genes were identified for downstream dimensionality reduction (Supplementary Fig. 3C), which were subsequently annotated into eight major cell lineages, including Fibroblasts, T cells, Epithelial cells, Endothelial cells, Macrophages, NK cells, B cells, and Mast cells (Fig. 9B, Supplementary Fig. 3D). Furthermore, intercellular communication network analysis via CellChat revealed that fibroblasts serve as the central communication hub, exhibiting the largest number and strongest interactions with all other cell types, particularly macrophages and epithelial cells (Supplementary Fig. 3E, F). Feature plot visualization across the UMAP space revealed a highly specific and heterogeneous expression pattern for PTTG1 (Fig. 9C). Quantitative analysis via violin plots further demonstrated that PTTG1 was predominantly overexpressed in malignant Epithelial cells (specifically enriched in cluster 20) and Macrophages (cluster 7) (Fig. 9D, E). To validate these findings within the native tissue context, we projected our data onto corresponding spatial transcriptomic sections. Compared with the histological architecture delineated by H&E staining (Fig. 9F), spatial mapping successfully localized the distinct cell types across the tissue slide (Fig. 9G). Crucially, the spatial expression profile of PTTG1 perfectly mirrored the scRNA-seq findings, showing robust and dense expression signals physically localized within the epithelial tumor parenchyma and regions densely infiltrated by macrophages (Fig. 9H). This powerful dual-omics approach intrinsically confirms that PTTG1 operates actively within malignant tumor cells while simultaneously reshaping the surrounding macrophage-dominated immune microenvironment.

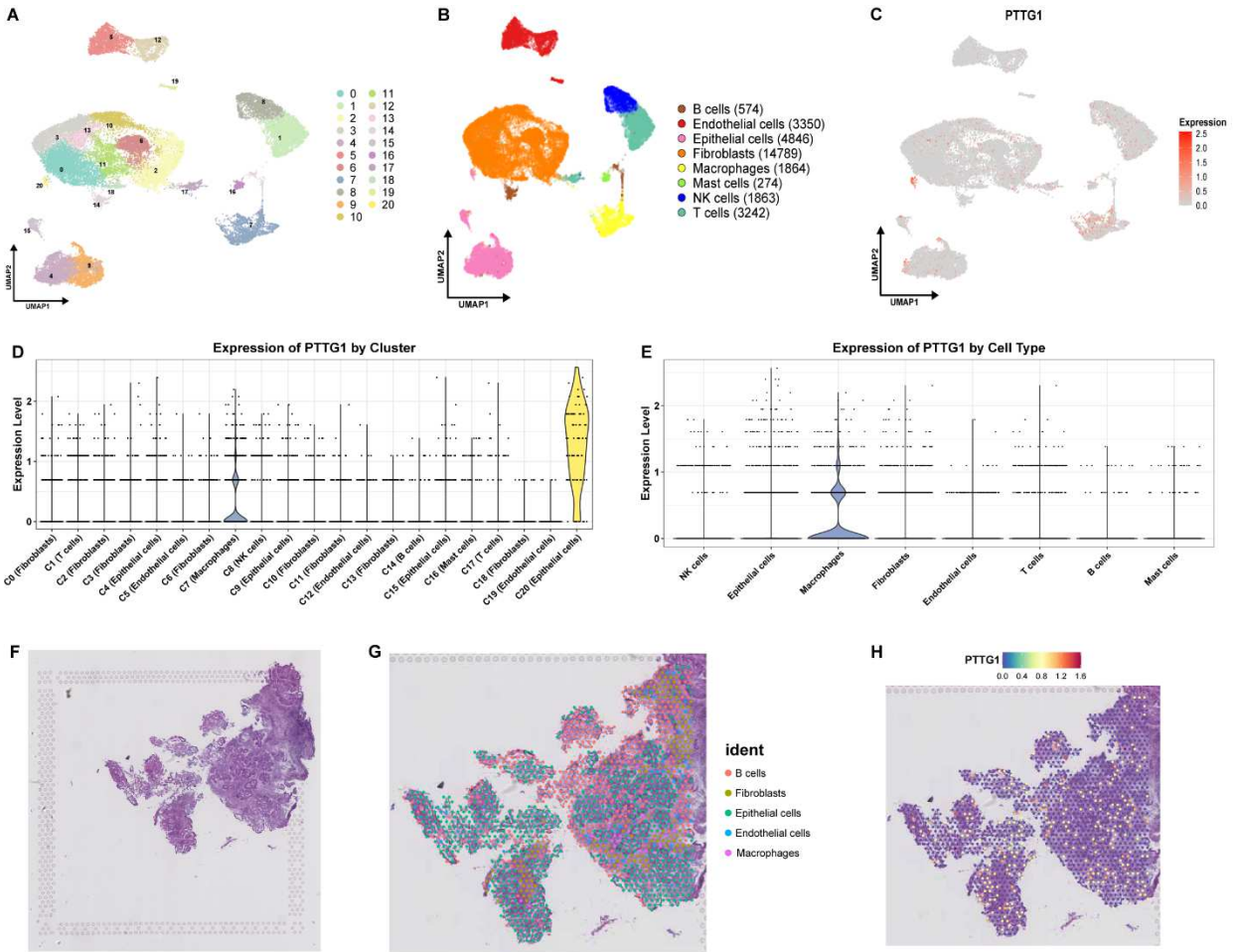


Figure 9. Single-cell and spatial transcriptomic landscape of PTTG1 expression in UCEC. (**A**) UMAP displaying the initial unsupervised clustering of scRNA-seq data into 21 distinct clusters. (**B**) UMAP visualization of the annotated single cells, categorized into eight major cell lineages. (**C**) Feature plot demonstrating the expression distribution of PTTG1 across the UMAP space, with red indicating high expression. (**D, E**) Violin plots detailing the expression levels of PTTG1 across individual clusters (**D**) and major annotated cell types (**E**), highlighting its significant enrichment in Epithelial cells (particularly cluster 20) and Macrophages. (F) Hematoxylin and Eosin (H&E) staining image of the UCEC spatial transcriptomics tissue section. (**G**) Spatial mapping of the identified cell types onto the tissue section architecture. (**H**) Spatial feature plot illustrating the physical localization and expression intensity of PTTG1, demonstrating its prominent enrichment in epithelial/tumor domains and macrophage-infiltrated regions.

In Silico Perturbation of PTTG1 Unveils Downstream Transcriptional and Metabolic Dependencies

To infer the direct causal regulatory network of PTTG1 in UCEC, we performed complementary in silico loss-of-function (virtual knockout) and gain-of-function (virtual overexpression) analysis. For the loss-of-function arm, PTTG1 was virtually depleted from the single-cell gene regulatory network (scGRN), and the resulting downstream perturbation was quantified by Z-scores. The virtual knockout of PTTG1 triggered a profound systemic shift in the downstream regulatory network, identifying a cohort of highly sensitive perturbed genes that were significantly up- or down-regulated upon PTTG1 suppression, such as PPP1R12B, AHCYL1, CFH, and GTF3C2 (Fig. 10A). Functional enrichment of these knockout-perturbed genes revealed massive disruptions in cell-

intrinsic biosynthetic machinery. GO analysis highlighted ribonucleoprotein complex biogenesis and RNA splicing in Biological Process (Fig. 10C), ribosomal subunit and spliceosomal complex in Cellular Component (Fig. 10D), and structural constituent of ribosome in Molecular Function (Fig. 10E). KEGG pathway analysis further revealed a strong dependency on specific metabolic pathways, notably glutathione metabolism and N-glycan biosynthesis (Fig. 10B).

In striking contrast, the overexpression of PTTG1 systematically activated immune-related transcriptional networks rather than cell-intrinsic pathways. A total of 31 genes were identified as significantly perturbed (FDR < 0.05), and remarkably, all 31 exhibited positive $\log_2$ fold changes, indicating a uniform upregulation response (Fig. 10F). The top-ranked differentially regulated genes included TSC22D3, IKZF1, TYROBP, and three MHC class II molecules: HLA-DRA, HLA-DQA1, and HLA-DPB1 (Fig. 10F). Additionally, the interleukin-2 receptor alpha chain (IL2RA), the pan-leukocyte marker PTPRC (CD45), the chemokine receptor CXCR4, the macrophage marker CD68, the integrin alpha X (ITGAX/CD11c), and the Fc receptor gamma chain (FCER1G) were prominently activated. KEGG enrichment analysis of these 31 positively perturbed genes revealed a striking and exclusive enrichment in immune regulatory processes (Fig. 10G), including Th1 and Th2 cell differentiation, Th17 cell differentiation, antigen processing and presentation, and phagocytosis. GO Biological Process analysis corroborated these findings, identifying positive regulation of lymphocyte activation, antigen processing and presentation of exogenous peptide antigen via MHC class II, and Fc receptor signaling pathway as the top enriched terms.

Collectively, these bidirectional in silico perturbation analyses reveal that PTTG1 functions as a dual-faceted oncogenic driver: intrinsically hijacking RNA splicing, ribosome biogenesis, and glutathione metabolism to sustain malignant proliferation, while extrinsically reprogramming the transcriptional landscape toward an immune-activated state dominated by MHC-II-mediated antigen presentation and lymphocyte signaling.

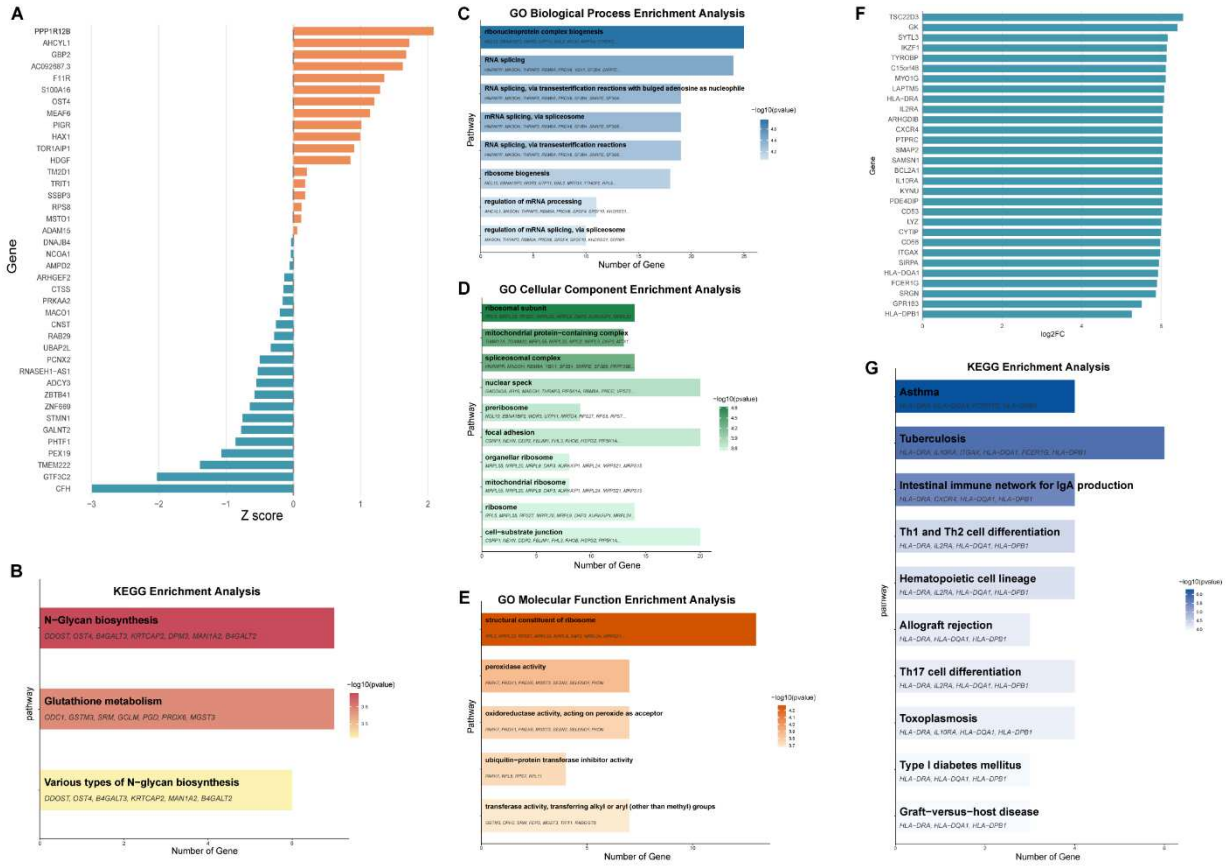


Figure 10. **In silico perturbation of PTTG1 reveals bidirectional transcriptional and functional consequences at single-cell resolution**.(**A–E**) Virtual knockout of PTTG1. (**A**) Z-scores of top significantly perturbed genes. (**B**) KEGG enrichment, highlighting N-glycan biosynthesis and glutathione metabolism. (**C–E**) GO enrichment across Biological Process (**C**), Cellular Component (**D**), and Molecular Function (**E**), revealing disruption of ribonucleoprotein complex biogenesis, RNA splicing, and ribosomal subunits.(**F** and **G**) Virtual overexpression of PTTG1. (**F**) $\log_2$ fold change of top perturbed genes (all positive, indicating uniform upregulation). (**G**) KEGG enrichment, dominated by immune-related pathways including Th1/Th2/Th17 differentiation, antigen processing and presentation, and phagocytosis.

Experimental Validation and CPTAC Proteomic Confirmation of PTTG1 in UCEC

Having established the prognostic and mechanistic significance of PTTG1 through comprehensive bioinformatics analyses, we next sought to experimentally validate its overexpression pattern using clinical specimens. Western blot analysis of six paired UCEC tumors and adjacent normal tissues confirmed that PTTG1 protein expression was significantly elevated in tumor specimens (Fig. 11A, B), with five of six cases (83.3%) exhibiting clear protein overexpression. Immunohistochemical (IHC) staining of PTTG1 was subsequently performed on five paired UCEC tumor and adjacent normal endometrial tissues to assess protein expression in situ. PTTG1 immunoreactivity was markedly stronger in tumor epithelial cells compared to the weak or absent staining in normal endometrial glands, with predominantly nuclear and moderate cytoplasmic localization, consistent with the protein expression pattern observed by WB (Fig. 11C). To achieve orthogonal validation at the transcript level within the same clinical specimens, total RNA from the six paired tissues was subjected to qRT-PCR. Consistent with the WB findings, PTTG1 mRNA was significantly

upregulated in tumor tissues (Fig. 11E). The degree of PTTG1 mRNA elevation demonstrated a positive, albeit not statistically significant at this sample size, correlation with the corresponding WB densitometry ratios (Pearson $r = 0.3690$, $p = 0.4717$; Fig. 11F). To further corroborate these tissue-level findings in an independent cohort, we queried the CPTAC-UCEC proteomic dataset. Consistent with our in-house validation, PTTG1 protein abundance was significantly higher in primary UCEC tumors compared to normal endometrium (Mann-Whitney U test, $p = 4.1 \times 10^{-5}$; Fig. 11D). Moreover, among the 42 patients with paired mRNA and protein data in the CPTAC cohort, PTTG1 transcript and protein levels were strongly correlated (Pearson $r = 0.822$, $p < 0.0001$; Fig. 11G), indicating faithful translation of transcriptomic upregulation to the functional protein level. Collectively, these concordant multi-platform results — spanning in-house WB, qRT-PCR, and IHC analyses, as well as independent CPTAC proteomic validation — firmly establish PTTG1 overexpression as a reproducible, protein-level oncogenic event in UCEC.

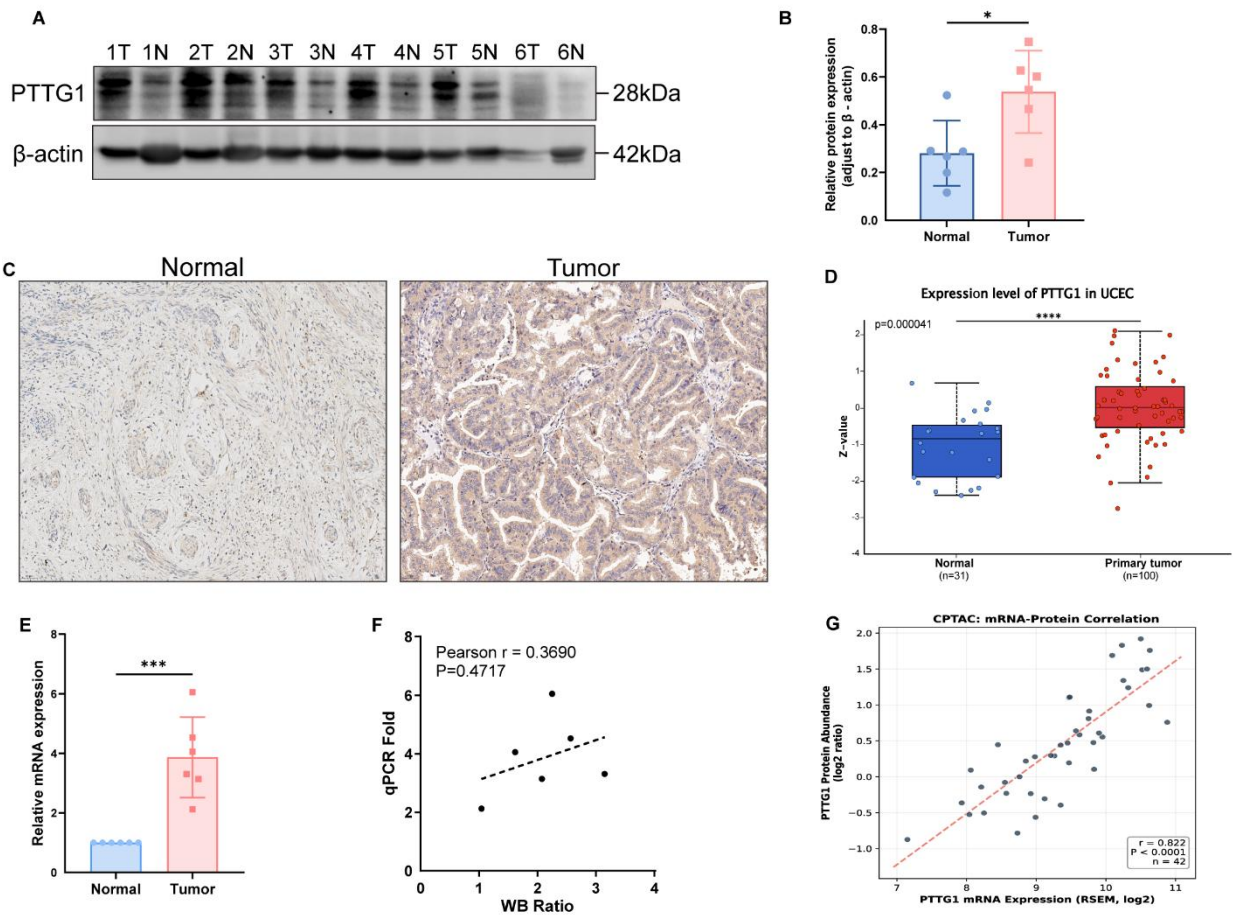


Figure 11. Experimental Validation and CPTAC Proteomic Confirmation of PTTG1 Overexpression in UCEC. (**A**) Western blot showing PTTG1 protein expression in six paired UCEC tumor (T) and adjacent normal (N) endometrial tissues. β-actin served as the loading control. (**B**) Quantification of PTTG1 protein expression normalized to β-actin in the six paired tissues (n=6). (**C**) Representative immunohistochemistry (IHC) staining of PTTG1 in paired UCEC tumor and adjacent normal endometrial tissues (n=5 pairs). Scale bar, 50 μm. (**D**) PTTG1 protein expression (Z-score) in normal endometrial tissues (n=31) versus primary UCEC tumors (n=100) from the CPTAC dataset, analyzed via UALCAN. (**E**) Relative PTTG1 mRNA expression measured by qRT-PCR in six paired UCEC tumor and adjacent normal tissues. Fold change (T/N) was calculated by the 2-ΔΔCT method with β-actin was used for normalization. (**F**) Correlation between PTTG1 mRNA levels (qRT-PCR, ΔCt) and PTTG1 protein levels (Western blot, normalized intensity) in the six paired tissue samples. Pearson r=0.3690, p=0.4717. (**G**) Correlation between PTTG1 mRNA (log_2 RSEM) and protein abundance (log_2 ratio) in CPTAC UCEC samples with matched profiles (n=42; cBioPortal, ucec_cptac_2020). Data in (B) and (E) are presented as mean ± SEM. *p < 0.05, **p < 0.01, ***p < 0.001, ****p < 0.0001; paired t-test for (B) and (E), Mann–Whitney U test for (D). Pearson correlation coefficients are reported in (F) and (G).

Discussion

UCEC remains one of the most prevalent gynecological malignancies worldwide, with its incidence and mortality rates steadily rising[32]. Despite continuous advancements in surgical and systemic therapeutic modalities, the prognosis for patients with advanced or recurrent UCEC remains dismal[33]. This clinical challenge is largely attributed to the high spatial and temporal heterogeneity of the tumors, as well as a critical shortage of precise prognostic biomarkers and therapeutic targets[34,35]. PTTG1 originally identified as a mammalian securin, plays an indispensable role in

regulating sister chromatid separation during mitosis and maintaining overall genomic stability[16]. Accumulating biological evidence has characterized PTTG1 as a potent oncogene, with its aberrant overexpression being implicated in the initiation, proliferation, and metastasis of various malignancies, including breast, prostate, and hepatocellular carcinomas[15]. However, its comprehensive multi-omics landscape, definitive prognostic value, and dynamic spatio-temporal role within the tumor immune microenvironment of UCEC have remained largely unexplored. In the present study, by systematically integrating bulk transcriptomics, advanced machine learning algorithms, single-cell RNA sequencing, and spatial transcriptomics, we robustly identified PTTG1 not merely as a core independent prognostic biomarker, but as a critical multidimensional driver that intrinsically fuels UCEC progression and extrinsically orchestrates an immunosuppressive microenvironment.

Intrinsically, our findings elucidate the multifaceted mechanisms by which PTTG1 drives the malignant proliferation and metabolic adaptation of UCEC cells. Through WGCNA and co-expression network analyses, we observed that PTTG1 is heavily integrated into pathways governing the cell cycle and mitosis. This perfectly aligns with its canonical function as a securin that regulates chromosomal segregation; however, its aberrant overexpression in UCEC appears to override critical cell cycle checkpoints, thereby fueling uncontrolled tumor replication. To move beyond mere transcriptomic correlation and establish a causal regulatory hierarchy, we uniquely applied an in silico virtual knockout algorithm at the single-cell resolution. Strikingly, the simulated depletion of PTTG1 triggered a systemic collapse in downstream targets predominantly associated with RNA splicing and ribosome biogenesis. Given that sustained malignant proliferation places an exponentially high demand on cellular protein synthesis, our virtual knockout evidence robustly suggests that PTTG1 acts as a pivotal upstream orchestrator. By hijacking the spliceosomal complexes and ribosomal translational machinery, PTTG1 ensures a constant supply of oncogenic proteins required for rapid tumor expansion[19]. Furthermore, the virtual knockout analysis uncovered a profound dependency of PTTG1-driven UCEC on specific stress-response pathways, particularly glutathione metabolism. As the master intracellular antioxidant, glutathione is critical for neutralizing reactive oxygen species (ROS) generated during hyperactive tumor growth[36,37]. Thus, PTTG1 not only accelerates cell division but also reprograms the metabolic and antioxidant defense systems to confer survival advantages and stress resistance to UCEC cells.

To further disentangle the dual mechanistic roles of PTTG1 as both an intrinsic proliferative driver and an extrinsic immune modulator, we complemented the virtual knockout analysis with a virtual overexpression simulation. Whereas the knockout exposed the cell-autonomous biosynthetic dependencies of PTTG1 — namely cell cycle progression, ribosome biogenesis, and glutathione metabolism — the overexpression remarkably triggered a uniform, systemic activation of immune-related transcriptional networks. The near-exclusive enrichment in MHC class II antigen presentation, Fc receptor signaling, and lymphocyte activation pathways suggest that PTTG1 overexpression has the potential to prime the tumor for immune recognition, potentially through enhanced antigen presentation machinery. This dichotomy — where PTTG1 intrinsically fuels proliferation while extrinsically engages immune signaling — reveals a nuanced mechanistic duality. It posits

that the clinically observed immunosuppressive phenotype in PTTG1-high UCEC patients may arise from a dominant pro-proliferative transcriptional program that outcompetes or actively suppresses the potentially immunogenic signals triggered by PTTG1 overexpression. This bidirectional causal evidence, derived from orthogonal in silico perturbation strategies, provides a uniquely comprehensive regulatory map of PTTG1's oncogenic architecture and reconciles its apparent paradox as both a proliferation driver and an immune network activator.

Extrinsically, our integrated multi-omics approach uncovered a critical role for PTTG1 in orchestrating an immunosuppressive cold tumor microenvironment. Through scRNA-seq and spatial transcriptomics, we made the striking observation that PTTG1 is not only expressed in the malignant epithelial cells but also profoundly enriched in tumor-associated macrophages. This physical and transcriptional spatial colocalization suggests a complex, bidirectional crosstalk between UCEC cells and the innate immune system. Furthermore, CellChat-mediated intercellular communication analysis revealed that fibroblasts serve as the central signaling hub within the UCEC microenvironment, exhibiting the strongest outgoing interactions with macrophages and epithelial cells. This suggests that fibroblast-driven paracrine signaling may constitute a critical mediator of the PTTG1-associated tumor-stroma-immune axis. Consistently, macroscopic TME evaluation using the ESTIMATE algorithm revealed that PTTG1-High patients suffered from a severe depletion of both stromal and active immune cell infiltration, resulting in an immune desert phenotype with exceptionally high tumor purity. Such highly immunosuppressive and cold TMEs are notoriously associated with therapeutic resistance, particularly to conventional immune checkpoint blockades. To bridge this critical translational gap, we leveraged large-scale pharmacogenomic profiling to identify alternative personalized therapeutic strategies. Our drug sensitivity predictions strikingly revealed that while PTTG1-High patients exhibit resistance to certain agents, they present remarkable, highly significant vulnerabilities to specific targeted therapies, most notably MEK inhibitors (e.g., Selumetinib and Trametinib) and MDM2 inhibitors (e.g., Nutlin-3a). The robust positive correlation between PTTG1 expression and MEK inhibitor sensitivity conceptually aligns with the hyperactive mitotic and proliferative state driven by PTTG1, as the MAPK/MEK signaling cascade is a central regulator of these very survival pathways. Consequently, our findings propose a paradigm shift: rather than relying on standard regimens, high-risk UCEC patients overexpressing PTTG1 may derive substantial clinical benefit from targeted kinase inhibition.

Notably, Selumetinib (AZD6244) and Trametinib (GSK1120212) warrant particular emphasis, as both compounds are selective, allosteric MEK1/2 inhibitors that converge on the very cell cycle machinery aberrantly activated by PTTG1 overexpression. The RAS–RAF–MEK–ERK signaling cascade serves as a critical conduit linking extracellular mitogenic stimuli to the core cell cycle apparatus, driving the G1/S transition through transcriptional upregulation of cyclin D1 and suppression of CDK inhibitors[38,39]. In the context of PTTG1-driven UCEC—where our co-expression network, functional enrichment, and in silico perturbation analyses collectively establish a profoundly hyperactive proliferative program, the MEK/ERK axis represents a mechanistically coherent therapeutic bottleneck. By locking MEK1/2 in an inactive conformation, Selumetinib and Trametinib abrogate ERK1/2 phosphorylation, effectively intercepting the proliferative output of

the PTTG1 oncogenic network at a central signaling node, resulting in G1 cell cycle arrest and apoptosis[40,41]. Clinically, Trametinib has demonstrated significant single-agent and combinatorial efficacy in BRAF-mutant melanoma and non-small cell lung cancer, and is currently under investigation in gynecologic malignancies, with a recent phase II/III trial demonstrating its activity in recurrent low-grade serous ovarian carcinoma, a tumor type that shares RAS-pathway dependency with certain aggressive UCEC subtypes[42]. Selumetinib has similarly shown clinical benefit in RAS-driven tumors and received FDA approval for NF1-associated plexiform neurofibromas[43]. The convergence of this established clinical experience with the robust biological rationale emerging from our multi-omics framework strongly positions MEK inhibition as a mechanistically grounded and clinically actionable therapeutic strategy for PTTG1-overexpressing, high-risk UCEC patients.

The experimental validation presented in this study provides multi-level, orthogonal confirmation of the computational framework established above. Western blot and qRT-PCR analyses of the six paired clinical specimens demonstrated that PTTG1 overexpression is a consistent and robust event at both the protein and mRNA levels, with five of six cases exhibiting concordant upregulation across the two measurement platforms. This bridges a critical gap between computational prediction and biological reality, substantiating that the PTTG1 upregulation identified in our multi-omics analysis is a genuine multi-layered oncogenic event rather than a transcriptomic artifact.

Furthermore, we validated PTTG1 protein overexpression in an independent external cohort using CPTAC proteomic data, which corroborated our tissue-level findings in a larger sample set. The strong mRNA-protein correlation observed in the CPTAC cohort supports the reliability of PTTG1 transcript-level analyses performed throughout this study. Meanwhile, our immunohistochemistry results confirmed that the elevated PTTG1 signal originates from tumor epithelium and is not confounded by stromal expression. The relatively weak mRNA-protein correlation in our clinical samples may reflect the limited sample size and highlights the necessity of multi-cohort validation. Taken together, the convergence of in-house experimental data with external CPTAC proteomic evidence provides robust, multi-layer confirmation of PTTG1 overexpression in UCEC.

Several limitations should be considered when interpreting these results. First, the experimental validation cohort was limited to six paired specimens for western blot/qPCR and five for immunohistochemistry, all from a single institution, which constrains statistical power and generalizability; larger multi-center validation is warranted. Second, the virtual gene perturbation analyses (scTenifoldKnock and scTenifoldNet) are computational predictions that require experimental confirmation through CRISPR-mediated approaches. Third, the CPTAC tumor-versus-normal comparison was derived as precomputed summary statistics from UALCAN rather than raw mass spectrometry data, and the paired mRNA-protein cohort comprised only 42 samples. Fourth, the single-cell RNA sequencing dataset (GSE173682) included five specimens, and the resolution of spatial transcriptomics may preclude detection of rare cell subpopulations. Fifth, drug sensitivity predictions were computationally inferred from GDSC/CTRP pharmacogenomic databases; the predicted

MEK inhibitor vulnerabilities require experimental validation in PTTG1-high versus PTTG1-low UCEC cell lines and patient-derived models before clinical translation.

Conclusions

In summary, this comprehensive integrative multi-omics analysis identifies PTTG1 as a profound and independent prognostic biomarker and a multidimensional oncogenic driver in UCEC. Intrinsically, PTTG1 fuels malignant cell proliferation through hyperactivation of cell cycle, ribosome biogenesis, and glutathione metabolism pathways. Extrinsically, it remodels the tumor immune microenvironment toward an immunosuppressive state characterized by immune cell depletion and macrophage crosstalk. Bidirectional in silico perturbation analyses revealed that PTTG1 loss disrupts core proliferative programs, while its overexpression activates immune-related transcriptional networks, including MHC class II antigen presentation and lymphocyte activation pathways. These computational findings were substantiated by multi-level experimental validation—Western blot, qRT-PCR, and immunohistochemistry in paired clinical UCEC specimens—and further corroborated by independent CPTAC proteomic analysis. Drug sensitivity predictions identified selective vulnerability to MEK inhibitors, including selumetinib and trametinib. Collectively, these findings provide a compelling rationale for PTTG1-guided prognostic stratification and MEK inhibitor-based targeted therapeutic strategies in high-risk UCEC.

List of abbreviations

UCEC: Uterine Corpus Endometrial Carcinoma;
WGCNA: Weighted Gene Co-expression Network Analysis;
DEG: Differentially Expressed Gene;
scRNA-seq: Single-cell RNA sequencing;
ST: Spatial Transcriptomics;
TME: Tumor Microenvironment;
TIME: Tumor Immune Microenvironment;
TCGA: The Cancer Genome Atlas;
GEO: Gene Expression Omnibus;
CPTAC: Clinical Proteomic Tumor Analysis Consortium;
LASSO: Least Absolute Shrinkage and Selection Operator;
SVM-RFE: Support Vector Machine-Recursive Feature Elimination;
ROC: Receiver Operating Characteristic;
AUC: Area Under the Curve;
CI: Confidence Interval;
HR: Hazard Ratio;
OS: Overall Survival;
PFI: Progression-Free Interval;
GO: Gene Ontology;
KEGG: Kyoto Encyclopedia of Genes and Genomes;
TAM: Tumor-Associated Macrophage;

Treg: Regulatory T cell;
NK: Natural Killer;
ICB: Immune Checkpoint Blockade;
IHC: Immunohistochemistry;
WB: Western Blot;
qRT-PCR: Quantitative Real-Time PCR;
FFPE: Formalin-Fixed Paraffin-Embedded.

Declarations

Ethics Statement

This study involved two main components. The bioinformatics analysis portion was based on publicly available and anonymized datasets from the TCGA, GEO, CPTAC, and cBioPortal databases. These databases have their own institutional review board approvals, and the original data were collected with informed consent from participants. Therefore, no additional ethical approval was required for the secondary analysis of these data. The clinical specimen validation component involved paired UCEC tumors and adjacent normal endometrial tissues collected from patients who underwent total hysterectomy at the First Affiliated Hospital of Zhengzhou University. Written informed consent was obtained from all participants, and this portion of the study was approved by the Institutional Ethics Committee of the First Affiliated Hospital of Zhengzhou University (Approval No: 2025-KY-0029). All methods were performed in accordance with the relevant guidelines and regulations, including the Declaration of Helsinki. Animal studies were not involved (N/A).

Consent for publication

Not applicable.

Availability of data and materials

All datasets used in this study are publicly available. Microarray datasets (GSE17025, GSE115810, GSE63678), single-cell RNA sequencing data (GSE173682), and spatial transcriptomics data (GSE203612) were obtained from the GEO database (https://www.ncbi.nlm.nih.gov/geo/). RNA sequencing and clinical data for the UCEC cohort were obtained from TCGA via the GDC Data Portal (https://portal.gdc.cancer.gov/). CPTAC-UCEC proteomic data were retrieved from cBioPortal (https://www.cbioportal.org/study/summary?id=ucec_cptac_2020) and UALCAN (http://ualcan.path.uab.edu/). Analysis code is available from the lead contact upon reasonable request. All analyses were performed using publicly available R packages as described in the method details.

Competing interests

The authors declare that they have no financial or non-financial competing interests.

Funding

This research was funded by the National Natural Science Foundation of China (NSFC) under Grant 82273229 (to R.X.-G) and Grant 82403060 (to L.L.-S); the Provincial-Ministrial Co-constructed Key Program of Henan Province under Grant SBGJ202302074 (to R.X.-G); and the Young Talent Support Program of Natural Science Foundation of Henan Province under Grant 242300420385 (to L.L.-S).

Authors' contributions

Dilimulati Yalikun: original draft preparation, methodology, software, formal analysis, investigation. Lulu Si: formal analysis and editing. Guo Zheng: Experimental validation, investigation.Yuxi Jin: resources, sample collection. Hanlin Fu: statistical analysis, investigation and validation. Ruixia Guo: supervision, project administration, funding acquisition.

Acknowledgements

The authors thank all members of the Department of Obstetrics and Gynecology, The First Affiliated Hospital of Zhengzhou University, for their support in clinical specimen collection. We also gratefully acknowledge TCGA, GEO, CPTAC, and cBioPortal consortia for making their data publicly available. We thank the Public Research Platform Management Center, First Affiliated Hospital of Zhengzhou University, for technical support.

Supporting information

Additional supporting information can be found online in the Supporting Information section.

References

1. Global cancer statistics 2022: GLOBOCAN estimates of incidence and mortality worldwide for 36 cancers in 185 countries - bray - 2024 - CA: a cancer journal for clinicians - wiley online library https://acsjournals.onlinelibrary.wiley.com/doi/full/10.3322/caac.21834.

2. Wu, J., Zhou, X., Ren, J., Zhang, Z., Ju, H., Diao, X., Jiang, S., and Zhang, J. (2023). Glycosyltransferase-related prognostic and diagnostic biomarkers of uterine corpus endometrial carcinoma. Comput. Biol. Med. *163*, 107164. https://doi.org/10.1016/j.compbiomed.2023.107164.

3. Liu, J., Hu, D., Lin, Y., Chen, X., Yang, R., Li, L., Zhan, Y., Bao, H., Zang, L., Zhu, M., et al. (2024). Early detection of uterine corpus endometrial carcinoma utilizing plasma cfDNA fragmentomics. BMC Med. *22*, 310. https://doi.org/10.1186/s12916-024-03531-8.

4. Liu, J., Geng, R., Yang, S., Shao, F., Zhong, Z., Yang, M., Ni, S., Cai, L., and Bai, J. (2021). Development and clinical validation of novel 8-gene prognostic signature associated with the proportion of regulatory T cells by weighted gene co-expression network analysis in uterine corpus endometrial carcinoma. Front. Immunol. *12*, 788431. https://doi.org/10.3389/fimmu.2021.788431.

5. Bozorgui, B., Kong, E.K., Luna, A., and Korkut, A. (2023). Mapping the functional interactions at the tumor-immune checkpoint interface. Commun. Biol. *6*, 462. https://doi.org/10.1038/s42003-023-04777-3.

6. Wang, Y., Liu, N., Guo, X., Han, R., Bai, J., Zhong, J., and Wang, Q. (2025). The immune microenvironment in endometrial carcinoma: Mechanisms and therapeutic targeting. Front. Immunol. *16*, 1586315. https://doi.org/10.3389/fimmu.2025.1586315.

7. López-Janeiro, Á., Villalba-Esparza, M., Brizzi, M.E., Jiménez-Sánchez, D., Ruz-Caracuel, I., Kadioglu, E., Masetto, I., Goubert, V., Garcia-Ros, D., Melero, I., et al. (2022). The association between the tumor immune microenvironments and clinical outcome in low-grade, early-stage endometrial cancer patients. J. Pathol. *258*, 426–436. https://doi.org/10.1002/path.6012.

8. De Visser, K.E., and Joyce, J.A. (2023). The evolving tumor microenvironment: From cancer initiation to metastatic outgrowth. Cancer Cell *41*, 374–403. https://doi.org/10.1016/j.ccell.2023.02.016.

9. Cassetta, L., and Pollard, J.W. (2023). A timeline of tumour-associated macrophage biology. Nat. Rev. Cancer *23*, 238–257. https://doi.org/10.1038/s41568-022-00547-1.

10. Li, Y., Qiu, H., Zhao, Z., Qi, F., and Cai, P. (2025). Single-cell technologies and spatial transcriptomics: Decoding immune low - response states in endometrial cancer. Front. Immunol. *16*, 1636483. https://doi.org/10.3389/fimmu.2025.1636483.

11. Erickson, B.K., Slomovitz, B., Powell, M., and Eskander, R.N. (2024). Top advances of the year: Uterine cancer. Cancer *130*, 2409–2412. https://doi.org/10.1002/cncr.35321.

12. Zhu, L., Yu, X., Wang, L., Liu, J., Qu, Z., Zhang, H., Li, L., Chen, J., and Zhou, Q. (2021). Angiogenesis and immune checkpoint dual blockade in combination with radiotherapy for treatment of solid cancers: Opportunities and challenges. Oncogenesis *10*, 47. https://doi.org/10.1038/s41389-021-00335-w.

13. Liao, J., Lu, X., Shao, X., Zhu, L., and Fan, X. (2021). Uncovering an organ's molecular architecture at single-cell resolution by spatially resolved transcriptomics. Trends Biotechnol. *39*, 43–58. https://doi.org/10.1016/j.tibtech.2020.05.006.

14. Mosquera Orgueira, A., González Pérez, M.S., Díaz Arias, J.Á., Antelo Rodríguez, B., Alonso Vence, N., Bendaña López, Á., Abuín Blanco, A., Bao Pérez, L., Peleteiro Raíndo, A., Cid López, M., et al. (2021). Survival prediction and treatment optimization of multiple myeloma patients using machine-learning models based on clinical and gene expression data. Leukemia *35*, 2924–2935. https://doi.org/10.1038/s41375-021-01286-2.

15. Rakoczy, K., Szymańska, N., Stecko, J., Kisiel, M., Sleziak, J., Gajewska-Naryniecka, A., and Kulbacka, J. (2025). The role of RAC2 and PTTG1 in cancer biology. Cells *14*, 330. https://doi.org/10.3390/cells14050330.

16. Wang, T., Zou, Y., Meng, H., Zheng, P., Teng, J., Huang, N., and Chen, J. (2024). Securin acetylation prevents precocious separase activation and premature sister chromatid separation. Curr. Biol. *34*, 1295-1308.e5. https://doi.org/10.1016/j.cub.2024.02.038.

17. Yu, J., Raia, P., Ghent, C.M., Raisch, T., Sadian, Y., Cavadini, S., Sabale, P.M., Barford, D., Raunser, S., Morgan, D.O., et al. (2021). Structural basis of human separase regulation by securin and CDK1–cyclin B1. Nature *596*, 138–142. https://doi.org/10.1038/s41586-021-03764-0.

18. Min, L., Feng, S., Liu, X., Zhang, Y., Zhao, M., Shi, H., Liu, X., and Wang, T. (2025). Emerging roles of PTTG1/securin in breast cancer. J. Cancer *16*, 4346–4356. https://doi.org/10.7150/jca.121650.

19. Zhou, Q., Li, L., Sha, F., Lei, Y., Tian, X., Chen, L., Chen, Y., Liu, H., and Guo, Y. (2023). PTTG1 reprograms asparagine metabolism to promote hepatocellular carcinoma progression. Cancer Res. *83*, 2372–2386. https://doi.org/10.1158/0008-5472.CAN-22-3561.

20. Perramón, M., and Jiménez, W. (2022). Pituitary tumor-transforming gene 1/delta like non-canonical notch ligand 1 signaling in chronic liver diseases. Int. J. Mol. Sci. *23*, 6897. https://doi.org/10.3390/ijms23136897.

21. Zhang, H., Chang, Z., Wang, C., Yuan, Z., Liu, Y., Wang, Y., Zhang, W., Zhong, Y., Wang, M., Zou, C., et al. (2024). SKA3/PTTG1/c-MYC signal loop drives the progression of colorectal cancer. Clin. Transl. Med. *14*, e1730. https://doi.org/10.1002/ctm2.1730.

22. Yang, K., Chen, M., Wu, Y., Duan, W., Huang, N., Zhao, X., and Cheng, D. (2025). Multi-omics integration identifies ASPH and PTTG1 as potential causal drivers of lung adenocarcinoma progression and immune evasion. Front. Immunol. *16*, 1689275. https://doi.org/10.3389/fimmu.2025.1689275.

23. Vergani, E., Teveroni, E., Mancini, F., Di Nicuolo, F., Raia, S., Chiloiro, S., Pierconti, F., Bianchi, A., Isidori, A.M., Pontecorvi, A., et al. (2025). Pituitary tumor-transforming gene 1 and endocrine cancers: An up-to-date review through history, current insights and future perspectives. Endocr. Relat. Cancer *32*, e240163. https://doi.org/10.1530/ERC-24-0163.

24. Gong, S., Wu, C., Duan, Y., Tang, J., and Wu, P. (2022). A comprehensive pan-cancer analysis for pituitary tumor-transforming gene 1. Front. Genet. *13*, 843579. https://doi.org/10.3389/fgene.2022.843579.

25. Wei, H., Ma, Y., Chen, S., Zou, C., and Wang, L. (2024). Multi-omics analysis identifies PTTG1 as a prognostic biomarker associated with immunotherapy and chemotherapy resistance. BMC Cancer *24*, 1315. https://doi.org/10.1186/s12885-024-13060-5.

26. Yang, T.-X., Zhang, J., Li, M.-J., Li, J.-D., Shen, S., Lu, T., Yang, G.-D., Wang, Q.-Y., Wang, Y., Luo, T., et al. (2026). Clonorchis sinensis promotes hepatocellular carcinoma progression via a potential PTTG1-β-catenin-c-MYC axis. Food Waterborne Parasitol. *42*, e00320. https://doi.org/10.1016/j.fawpar.2026.e00320.

27. Vlotides, G., Eigler, T., and Melmed, S. (2007). Pituitary tumor-transforming gene: Physiology and implications for tumorigenesis. Endocr. Rev. *28*, 165–186. https://doi.org/10.1210/er.2006-0042.

28. Kanehisa, M. (2000). KEGG: Kyoto encyclopedia of genes and genomes. Nucleic Acids Res. *28*, 27–30. https://doi.org/10.1093/nar/28.1.27.

29. Kanehisa, M., Furumichi, M., Sato, Y., Kawashima, M., and Ishiguro-Watanabe, M. (2023). KEGG for taxonomy-based analysis of pathways and genomes. Nucleic Acids Res. *51*, D587–D592. https://doi.org/10.1093/nar/gkac963.

30. Osorio, D., Zhong, Y., Li, G., Xu, Q., Yang, Y., Tian, Y., Chapkin, R.S., Huang, J.Z., and Cai, J.J. (2022). scTenifoldKnk: An efficient virtual knockout tool for gene function predictions via single-cell gene regulatory network perturbation. Patterns *3*, 100434. https://doi.org/10.1016/j.patter.2022.100434.

31. Osorio, D., Zhong, Y., Li, G., Huang, J.Z., and Cai, J.J. (2020). scTenifoldNet: A machine learning workflow for constructing and comparing transcriptome-wide gene regulatory networks from single-cell data. Patterns *1*, 100139. https://doi.org/10.1016/j.patter.2020.100139.

32. Siegel, R.L., Giaquinto, A.N., and Jemal, A. (2024). Cancer statistics, 2024. CA. Cancer J. Clin. *74*, 12–49. https://doi.org/10.3322/caac.21820.

33. Mirza, M.R., Chase, D.M., Slomovitz, B.M., dePont Christensen, R., Novák, Z., Black, D., Gilbert, L., Sharma, S., Valabrega, G., Landrum, L.M., et al. (2023). Dostarlimab for primary advanced or recurrent endometrial cancer. N. Engl. J. Med. *388*, 2145–2158. https://doi.org/10.1056/NEJMoa2216334.

34. Xi, X., Gong, X., Liu, Y., Cui, B., Xia, C., Qin, S., and Du, J. (2025). SLC2A1 and MPST as diagnostic and prognostic biomarkers of potential endometrial cancer. Front. Immunol. *16*, 1575916. https://doi.org/10.3389/fimmu.2025.1575916.

35. Wu, E., Fan, X., Tang, T., Li, J., Wang, J., Liu, X., Zungar, Z., Ren, J., Wu, C., and Shen, B. (2022). Biomarkers discovery for endometrial cancer: A graph convolutional sample network method. Comput. Biol. Med. *150*, 106200. https://doi.org/10.1016/j.compbiomed.2022.106200.

36. Jia, S., Ke, S., Tu, L., Chen, S., Luo, B., Xiong, Y., Li, Y., Wang, P., and Ye, S. (2023). Glutathione/pH-responsive copper-based nanoplatform for amplified chemodynamic therapy through synergistic cycling regeneration of reactive oxygen species and dual glutathione depletion. J. Colloid Interface Sci. *652*, 329–340. https://doi.org/10.1016/j.jcis.2023.08.043.

37. Peng, S.-Y., Liu, X.-H., Chen, Q.-W., Yu, Y.-J., Liu, M.-D., and Zhang, X.-Z. (2022). Harnessing in situ glutathione for effective ROS generation and tumor suppression via nanohybrid-mediated catabolism dynamic therapy. Biomaterials *281*, 121358. https://doi.org/10.1016/j.biomaterials.2021.121358.

38. The ERK1/2 mitogen-activated protein kinase pathway as a master regulator of the G1- to S-phase transition | oncogene https://www.nature.com/articles/1210414.

39. Chambard, J.-C., Lefloch, R., Pouysségur, J., and Lenormand, P. (2007). ERK implication in cell cycle regulation. Biochim. Biophys. Acta BBA - Mol. Cell Res. *1773*, 1299–1310. https://doi.org/10.1016/j.bbamcr.2006.11.010.

40. MEK1 and MEK2 inhibitors and cancer therapy: The long and winding road | nature reviews cancer https://www.nature.com/articles/nrc4000.

41. The clinical development of MEK inhibitors | nature reviews clinical oncology https://www.nature.com/articles/nrclinonc.2014.83.

42. Gershenson, D.M., Miller, A., Brady, W.E., Paul, J., Carty, K., Rodgers, W., Millan, D., Coleman, R.L., Moore, K.N., Banerjee, S., et al. (2022). Trametinib versus standard of care in patients with recurrent low-grade serous ovarian cancer (GOG 281/LOGS): An international, randomised, open-label, multicentre, phase 2/3 trial. The Lancet *399*, 541–553. https://doi.org/10.1016/S0140-6736(21)02175-9.

43. Gross, A.M., Wolters, P.L., Dombi, E., Baldwin, A., Whitcomb, P., Fisher, M.J., Weiss, B., Kim, A., Bornhorst, M., Shah, A.C., et al. (2020). Selumetinib in children with inoperable plexiform neurofibromas. N. Engl. J. Med. *382*, 1430–1442. https://doi.org/10.1056/NEJMoa1912735.

Figure legends

Figure 1. Batch effect correction and differential expression analysis.

(A) PCA plots before (left) and after (right) batch effect correction of the three integrated GEO datasets. (B) Box plots showing gene expression distribution before and after batch correction. (C) Volcano plot of differentially expressed genes (DEGs) between UCEC tumor and normal tissues ($|\log_2 FC| > 1$, adjusted $p < 0.05$). (D) Heatmap of the top 50 DEGs. (E) KEGG pathway enrichment analysis of DEGs. (F) GO enrichment analysis of DEGs.

Figure 2. Weighted gene co-expression network analysis (WGCNA).

(A) Scale-free topology fit index across soft-thresholding powers. (B) Mean connectivity analysis. (C) Gene dendrogram with module color assignment. (D) Module-trait relationship heatmap. (E, F) Scatter plots of Gene Significance vs. Module Membership for the turquoise (E) and yellow (F) modules. (G) Venn diagram of DEGs and WGCNA module genes. (H) GO enrichment analysis of consensus candidate genes. (I) KEGG pathway enrichment analysis of consensus candidate genes.

Figure 3. Machine learning-based core gene screening.

(A) LASSO coefficient profiles. (B) Cross-validation for optimal lambda selection. (C) SVM-RFE accuracy across feature subsets. (D) SVM-RFE error rate across feature subsets. (E) XGBoost

SHAP summary plot. (F) XGBoost feature importance ranking. (G) Boruta Z-score distribution. (H) Boruta decision plot. (I) Venn diagram of overlapping genes selected by all four algorithms.

Figure 4. Expression validation, diagnostic value, and prognostic significance of core genes.

(A) Box plots showing differential expression of PNP, CDC20, PTTG1, S100A11, and KLF5 in TCGA-UCEC. (B) ROC curves for the five core genes. (C–G) Kaplan-Meier overall survival curves for PNP (C), CDC20 (D), PTTG1 (E), S100A11 (F), and KLF5 (G). (H) Kaplan-Meier progression-free interval curve for PTTG1.

Figure 5. Correlation of PTTG1 expression with clinicopathological features in UCEC.

(A) Comprehensive heatmap of PTTG1 expression across clinicopathological features. (B) PTTG1 expression by age. (C) PTTG1 expression by overall survival status. (D) PTTG1 expression by histological subtype. (E) PTTG1 expression by FIGO stage. (F) PTTG1 expression by tumor stage (I/II vs. III/IV). (G) PTTG1 expression by histological grade. (H) PTTG1 expression by BMI category.

Figure 6. PTTG1 co-expression network and functional enrichment in UCEC.

(A–C) Scatter plots of top positively co-expressed genes with PTTG1: CDC25C (A), UBE2C (B), and CDCA3 (C). (D–F) Scatter plots of top negatively co-expressed genes: FAM189A2 (D), FCER1A (E), and IGFBP4 (F). (G) GO enrichment analysis of PTTG1 co-expressed genes. (H) KEGG pathway enrichment analysis of PTTG1 co-expressed genes.

Figure 7. Tumor immune microenvironment remodeling associated with PTTG1 in UCEC.

(A) CIBERSORT immune cell composition in PTTG1-high and PTTG1-low groups. (B) Global Spearman correlation matrix between PTTG1 expression and immune cell subtypes. (C) Detailed correlations between PTTG1 and individual immune cell subtypes. (D) ESTIMATE scores (StromalScore, ImmuneScore, ESTIMATEScore) in PTTG1-high vs. PTTG1-low groups. Data are presented as box plots with Wilcoxon rank-sum test p values.

Figure 8. Drug sensitivity prediction guided by PTTG1 expression.

(A) Heatmap of drug sensitivity differences between PTTG1-high and PTTG1-low groups. (B) Top 10 drugs with greatest sensitivity differences between groups. (C–E) Box plots of predicted IC_{50} values for Selumetinib (C), Trametinib (D), and Nutlin-3a (E). (F) Spearman correlation between PTTG1 expression and Selumetinib sensitivity. (G–I) Box plots of drugs with increased resistance in the PTTG1-high group. (J) Spearman correlation between PTTG1 expression and AZD5991 sensitivity.

Figure 9. Single-cell and spatial transcriptomic characterization of PTTG1 in UCEC.

(A) UMAP visualization of 21 single-cell clusters. (B) UMAP plot annotated by eight major cell lineages. (C) Feature plot showing PTTG1 expression across the UMAP space. (D) Violin plot of PTTG1 expression across cell clusters. (E) Dot plot of PTTG1 expression by cell type. (F) H&E-stained tissue section. (G) Spatial mapping of cell type annotations on tissue section. (H) Spatial feature plot of PTTG1 expression.

Figure 10. In silico perturbation analysis of PTTG1.

(A) Volcano plot of perturbed genes after virtual PTTG1 knockout. (B) KEGG enrichment of knockout-perturbed genes. (C–E) GO enrichment of knockout-perturbed genes: Biological Process (C), Cellular Component (D), and Molecular Function (E). (F) Volcano plot of differentially expressed genes after virtual PTTG1 overexpression. (G) KEGG enrichment of overexpression-perturbed genes.

Figure 11. Experimental validation and CPTAC proteomic confirmation of PTTG1 in UCEC.

(A) Representative Western blot images of PTTG1 in six paired UCEC tumor (T) and adjacent normal (N) tissues. (B) Densitometric quantification of Western blot results (n = 6). (C) Representative immunohistochemistry images of PTTG1 in UCEC tumor and adjacent normal tissues. Scale bar: 100 μm. (D) CPTAC proteomic comparison of PTTG1 protein abundance between UCEC tumors (n = 100) and normal endometrium (n = 31). (E) qRT-PCR analysis of PTTG1 mRNA expression in six paired specimens. (F) Correlation between Western blot densitometry ratios and qRT-PCR fold changes. (G) Pearson correlation between PTTG1 mRNA and protein levels in the CPTAC cohort (n = 42).

Supplementary Files

This is a list of supplementary files associated with this preprint. Click to download.

- SupplementaryFiles.docx
- UncroppedWBimages.docx